Design and Development of Instrumented Foot Form for Testing of Metatarsal Protective Footwear

by

Anandita Gautam

A thesis
presented to the University of Waterloo
in fulfillment of the
thesis requirement for the degree of

Master of Applied Science
in
Mechanical and Mechatronics Engineering

Waterloo, Ontario, Canada, 2025

© Anandita Gautam 2025

Author's Declaration

I hereby declare that I am the sole author of this thesis. This is a true copy of the thesis, including any required final revisions, as accepted by my examiners.

I understand that my thesis may be made electronically available to the public.

Abstract

Protective footwear with metatarsal guards can play a critical role in preventing high-energy impact injuries to the foot. Currently, there is a wide variety of different metatarsal guard types, each of which must pass impact testing standards before being used. These current impact testing standards to assess the efficacy of protective footwear, such as ASTM F2412, often use deformation of an internal material like wax as the performance indicator for metatarsal guards. However, previous studies have shown that deformation is not a great predictor of metatarsal fracture injury risk. Therefore, the overall goal of this work was to develop and validate a biofidelic instrumented foot surrogate for evaluating the impact performance of metatarsal protective equipment. A combination of computational and experimental methods were first used to identify a surrogate material that demonstrates a similar force-deformation response to the human foot. Next, design for additive manufacturing parameters, such as lattice structures, infill density, and unit cell size, were used to produce a foot form with a biofidelic impact response. This design process used an iterative methodology to develop three prototypes of additively manufactured surrogates using engineered hyperelastic material and embedded load cells.

A series of drop tower tests were conducted using ASTM methodology, and the force and deformation for each prototype was compared to cadaveric data reported in the literature. Three types of metatarsal guards were drop tested with the prototypes, and transmitted forces were recorded through an embedded force measurement system. Results from impact testing showed that all developed prototypes provided a closer match to cadaveric force-deformation behaviour, with Prototypes I and III performing slightly better. Metatarsal guard performance results were limited as the load-sensing equipment was overloaded. Prototype I's load-sensing method was unreliable. Prototype II reported the worst performance for soft metatarsal guard footwear. Prototype III demonstrated that soft and hard metatarsal guards offer better protection than boots without guards.

In conclusion, this study presented a novel foot surrogate for metatarsal impact resistance testing. Further studies are required to refine the design to improve the force-measurement system and ensure a better fit of the foot surrogate inside protective footwear.

Acknowledgements

I would like to express my deepest gratitude to my supervisors, Dr. Naveen Chandrashekar and Dr. Stewart McLachlin, for their mentorship, encouragement, and support throughout the course of my master's degree. Their guidance and insightful feedback were instrumental in shaping the direction of this work and in helping me overcome the challenges encountered during this project.

I am sincerely thankful to the team at ASTM for their collaboration and support throughout this project. Their contributions, resources, and commitment to advancing research played a significant role in the successful execution of this work.

I would like to express my sincere gratitude to the University of Waterloo for providing me with the opportunity to pursue a Master of Applied Science. My heartfelt thanks go to my labmates at the Structural Biomechanics Lab and the Orthotron Lab for their valuable discussions, technical assistance, and friendship during this journey.

Finally, thank you to my family and friends for their unwavering belief in me. To my sister Anubha, thank you for being the best sister I could ask for and supporting me every step of the way. To my dad, thank you for showing me how to navigate life's hurdles. To my mom, thank you for teaching me how to take one step at a time and live fully. To my grandparents, thank you for being my biggest supporters. This work would not have been possible without you.

Dedication

To my grandfather, grandmother, my parents, and my sister

Table of Contents

Author's Declaration ii

Abstract iii

Acknowledgements iv

Dedication v

List of Figures ix

List of Tables xii

1 Introduction 1

1.1 Project Motivation 1

1.2 Thesis Objectives 3

1.3 Thesis Overview 3

2 Background 4

2.1 Anatomical Background 4

2.1.1 Nomenclature 4

2.1.2 Foot Anatomy 5

2.2 Mechanical Behaviour of Metatarsals 8

2.3 Foot Injuries . . . 9
2.4 Metatarsal Guards . . . 10
2.5 Review of Standards . . . 11
2.5.1 Protective Footwear Standards . . . 11
2.6 Development of Human Body Surrogates . . . 13
2.7 Additive Manufacturing . . . 15
2.8 Design for Additive Manufacturing . . . 17
2.8.1 Design Aspects . . . 18
2.8.2 Design Considerations . . . 21
2.8.3 Applications of Design for Additive Manufacturing . . . 22
2.9 Knowledge Gaps and Opportunities . . . 24

3 Identification of a Biofidelic Foot Form Material 25
3.1 Evaluation Benchmark . . . 25
3.2 Experimental Setup . . . 26
3.3 Computational Pre-Screening . . . 28
3.3.1 Development of FE Model . . . 28
3.3.2 Experimental Verification of Alternate Rubber Material . . . 31
3.4 Additive Manufacturing Approach . . . 32
3.4.1 Fused Deposition Modelling (FDM) . . . 33
3.4.2 Sterolithography (SLA) . . . 36
3.5 Chapter Summary . . . 39

4 Design of Instrumented Foot Form for Force Measurement 41
4.1 Design Framework . . . 41
4.2 Design Requirements . . . 42
4.3 Prototype I . . . 43
4.3.1 Conceptual Design . . . 43

4.3.2 Manufacturability of Prototype I . . . 45
4.3.3 Experimental Testing . . . 47
4.3.4 Limitations of Prototype I . . . 49
4.4 Prototype II . . . 50
4.4.1 Two Load Cell System and Validation . . . 51
4.4.2 Conceptual Design . . . 53
4.4.3 Manufacturability of Prototype II . . . 54
4.4.4 Experimental Testing . . . 55
4.4.5 Limitations of Prototype II . . . 60
4.5 Prototype III . . . 60
4.5.1 Conceptual Design . . . 60
4.5.2 Manufacturability of Prototype III . . . 62
4.5.3 Experimental Testing . . . 63
4.6 Chapter Summary . . . 68

5 Discussion **69**
5.1 Computational and Experimental Approaches in Material Selection . . . 69
5.2 Iterative Design of Instrumented Foot Form . . . 71
5.3 Performance of Instrument Foot Forms . . . 74
5.4 Summary . . . 77

6 Thesis Conclusions **78**
6.1 Summary . . . 78
6.2 Limitations and Future Work . . . 79

References **81**

List of Figures

1.1 External metatarsal guard used for metatarsal protection 2

2.1 Anatomical Planes and Directions of the Human Body 5
2.2 Bones of a Human Foot 6
2.3 Medial Longitudinal Arch Models 8
2.4 Different metatarsal guard types 10
2.5 ASTM Metatarsal Footwear Impact Test Apparatus 12
2.6 Foot Form Surrogate from CSA 13
2.7 Examples of Surrogates 14
2.8 AM process chain 15
2.9 Schematic representation of SLA 16
2.10 Schematic representation of FDM 16
2.11 Design for AM Framework 17
2.12 Difference between Unit Cell and Lattice 19
2.13 Lattice Patterns with increasing infill densities 20
2.14 Effect of Build Orientation on Anisotropy 21
2.15 Accuracy in xy plane and z axis 22

3.1 Fracture-risk curve of metatarsals based on impact energy 26
3.2 (a) Data Acquisition System (b) Drop Tower Setup 27
3.3 FE Model Setup: A-rigid plate, B-foot model, C-indentor, D-point mass (6.2kg) 29

3.4 Force deformation response of vulcanized rubber vs cadaver at 33J impact energy . . . 31
3.5 Rubber Blocks: A-Neoprene 60A , B-Neoprene 50A . . . 32
3.6 Latticed TPU sections . . . 34
3.7 Force-deformation response of latticed Ninjaflex ® TPU vs cadaver at 33 J impact energy . . . 36
3.8 Resin latticed parts: A-truncated cube 80%, B-cubic lattice 70% and C - 55% cubic lattice . . . 38
3.9 Force-deformation response of latticed flexible 80A resin vs latticed Ninjaflex ® TPU at 33 J impact energy . . . 39

4.1 Design Framework Methodology . . . 42
4.2 Concept Design of Prototype I . . . 44
4.3 Prototype I . . . 45
4.4 Procedure to place the Prototype I inside the boot for testing . . . 47
4.5 Force-deformation response of Prototype I vs Cadaver at 33 J impact energy 48
4.6 Metatarsal injury risk curves based on applied impact energy and force . . 49
4.7 Load sensing area of a single load cell system . . . 50
4.8 Two Load Cell System . . . 51
4.9 Section View of Load Cell Validation Setup . . . 52
4.10 Concept Design of Prototype II . . . 53
4.11 Prototype II . . . 54
4.12 Force-deformation response of Prototype II vs Cadaver . . . 55
4.13 Load Cell Force vs Energy Response Accuracy - Prototype II . . . 56
4.14 Load Cell Force vs Energy Response Repeatability - Prototype II . . . 56
4.15 Safety footwear evaluated for metatarsal guard performance . . . 58
4.16 Transmitted mean force at 50 J for each boot using Prototype II . . . 59
4.17 Concept Design of Prototype III . . . 61
4.18 Prototype III . . . 62

4.19 Force-deformation response of Prototype III vs Cadaver 63
4.20 Transmitted mean force at 10 J for each boot using Prototype III 66
4.21 Transmitted mean force at 20 J for each boot using Prototype III 66

5.1 Three Prototypes: A- Prototype I, B- Prototype II, C- Prototype III . . . 72
5.2 Arches differences between Prototypes II and III 72
5.3 Difference between material width in Prototype I (B) and Prototype II (A) 73
5.4 Load sensing area difference between single vs dual load cell system 75

List of Tables

2.1 FDM vs. SLA: Advantages and Limitations 17

3.1 Impact Tower Key Components and Specifications 27
3.2 Materials and their properties for FE Study 30
3.3 Foot sections printed with TPU of varying infill densities and patterns . . . 34
3.4 Optimum settings for 3D printing in PrusaSlicer with Ninjaflex ® 35
3.5 Cuboids printed with Flexible 80A of varying infill densities, lattice patterns, and unit cell size 37

4.1 Design Requirements for the Instrumented Foot Form 43
4.2 Manufacturing Specifications - Prototype I 46
4.3 Benchmark Testing for Prototype I 49
4.4 Two Load Cell Validation Results at Three Different Impact Points 52
4.5 Manufacturing Specifications - Prototype II 54
4.6 Benchmark Testing for Prototype II 57
4.7 Specifications of safety footwear evaluated for metatarsal guard performance 58
4.8 Transmitted force at 100 J, for each boot using Prototype II 59
4.9 Manufacturing Specifications - Prototype III 62
4.10 Load Cell Response at various impact energies- Prototype III 64
4.11 Benchmark Test at 20J - Prototype III 65
4.12 Transmitted force at 30 J, for each boot using Prototype III 67
4.13 Transmitted force at 50 J, for each boot using Prototype III 67

Chapter 1

Introduction

1.1 Project Motivation

Foot injuries are one of the most common workplace-related injuries and are associated with significant morbidity, reduced mobility, and loss of productivity. According to the National Safety Council, over 151,000 work-related foot injuries were reported in the United States between 2021 and 2022, many of which resulted in restricted duties or absence from work [1]. A majority of these injuries involve metatarsal fractures, which account for approximately 35-55% of all foot and ankle fractures [2, 3]. It was found that high-energy trauma, such as direct impacts from falling objects, is the leading cause of these fractures [4]. To mitigate these injuries, footwear manufacturers have developed metatarsal guards for impact protection in safety footwear (Figure 1.1).

Standards development organizations (SDOs) like ASTM International have developed metatarsal impact testing methods as part of safety footwear standards, such as ASTM F2412 [5], which aim to evaluate the performance of protective devices like metatarsal guards. For metatarsal impact testing, the ASTM F2412 standard describes using a wax material molded inside a boot and measuring the wax deformation caused by a simulated workplace impact energy of 101.75J, which is equivalent to a 50 lbs mass dropped from approximately waist height (0.5 m). Similarly, CSA Standards [6] also adopt deformation as the primary evaluation criterion, using plasticene materials rather than wax for measuring deformation following impact. However, the deformation-based criteria adopted in these current standards lacks supporting research that links deformation to metatarsal fracture risk. Moreover, molded wax foot forms used by ASTM are not reusable following impact, and their mechanical response varies with preparation conditions, cooling rate, and ambient



Figure 1.1: External metatarsal guard used for metatarsal protection

temperature, so successive foot forms may not behave the same. As a result, current impact testing methodologies of SDOs does not easily or effectively capture the protective efficacy of metatarsal guards.

Synthetic material surrogates for human tissues, like the wax used in ASTM F2412, are commonly used in defence, automotive, and medical industries to assess the effectiveness of personal protective equipment (PPE). However, these surrogates often have limited similarities to human anatomy in terms of geometry, material, and mechanical behaviour. As a result, there is a growing need to improve the bio-fidelity of surrogates used in safety standards. Recent advancements in additive manufacturing could offer a promising solution to this problem. The use of 3D printing principles allows for the creation of engineered material that can mimic the mechanical response of anatomical structures. Additionally, because the space inside a safety boot is limited, the use of modular force sensors may offer a more practical, reusable option than deformation sensors and can be embedded within the surrogate to record impact forces. By combining an additively manufactured engineered material with an embedded force-measurement system, it is possible to develop a biofidelic foot form capable of obtaining the force transferred to the metatarsals during repeated impact trials. An instrumented foot form would help to address the re-usability limitations of the current ASTM standards and provide a more reliable method for assessing

the protective performance of metatarsal guards.

1.2 Thesis Objectives

The overall objective of this research was to design and validate a modular, instrumented foot form capable of repeatable impact force measurement that closely replicates the biomechanical response of a cadaveric foot when subjected to impact testing for metatarsal guard evaluation. The specific objectives were then as follows:

1. Identification of an easy to manufacture, biofidelic material that reproduces cadaveric force-deformation response.
2. Development of an accurate and repeatable method to measure impact force within the metatarsal region of the foot.
3. Validation of the developed foot form via ASTM-aligned impact testing of safety footwear with embedded metatarsal guards.

1.3 Thesis Overview

This thesis is structured into five chapters. Chapter 1 (Introduction) presents the motivation behind the research and outlines its objectives. Chapter 2 (Background) explores prior studies on anatomy, current testing standards, anatomical surrogates, and Design for Additive Manufacturing (DfAM) principles and applications. Chapter 3 (Material Selection) details the material selection process through computational and experimental studies. Chapter 4 (Design of Instrumented Foot Form) showcases the process of developing three prototypes, the integration of the force measurement method, and their validation. Chapter 5 (Discussion) summarizes the key findings, highlights the limitations of the study, and proposes future directions for refining the foot form and standardizing its adoption. Lastly, Chapter 6 (Conclusion) presents a brief conclusion for this study, addresses the gaps and limitations, and provides recommendations for future work.

Chapter 2

Background

2.1 Anatomical Background

A thorough understanding of human foot anatomy is required to understand the design considerations of the instrumented foot form. The subsequent sections discuss anatomical nomenclature, foot anatomy, with a specific focus on the metatarsal region, and biomechanics of foot loading.

2.1.1 Nomenclature

The anatomy of the human body is described using planes and directional pairs as shown in Figure 2.1. The three planes used in anatomy are *sagittal*, *coronal* (also known as frontal), and *transverse* planes. The sagittal planes divide the body into right and left halves. *Flexion* and *extension* movements occur primarily in this plane. The coronal plane divides the human body between the front and back halves. The primary movements that happen in this plane are *abduction* and *adduction*. Lastly, the transverse plane differentiates the upper and lower segments of the body, and movements in this plane are classified as *internal/external rotation*.

In addition, the direction pairs describe the relative positions of body parts. *Proximal* and *distal* refer to whether a structure is located closer to or farther from the point of origin. *Medial* and *lateral* indicate whether the structure is oriented toward or away from the body's midline. *Anterior* and *posterior* denote whether the anatomical feature lies toward the front or the back of the body, respectively.

Common anatomical terms used to describe the foot help provide clear orientation and localization when discussing injuries, treatments, or anatomy. Two important terms used to describe surfaces of the foot are dorsal and plantar. The plantar surface refers to the sole, which is the part in contact with the ground when standing. The dorsal surface is the top of the foot, which faces upward when standing.

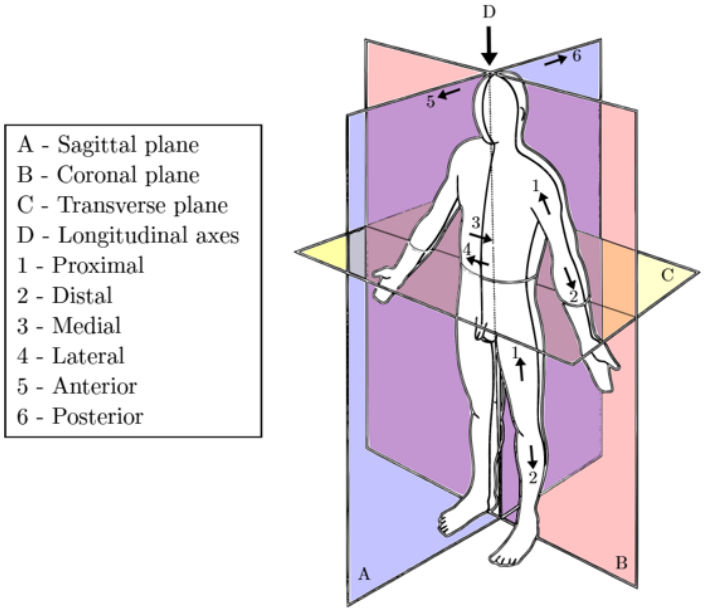


Figure 2.1: Anatomical Planes and Directions of the Human Body
(Adapted from [7])

2.1.2 Foot Anatomy

Bones and Ligaments

The human foot is a complex anatomical structure comprising 26 bones (Figure 2.2), which can be categorized into three regions: the hindfoot, midfoot, and forefoot. This skeletal framework provides stability, mobility, and support during standing, walking, and running. The hindfoot and midfoot together form the *tarsus*, which consists of seven tarsal bones that contribute to the foot's stability and flexibility [8]. The hindfoot consists of two major bones: the *talus* and the *calcaneus*. The talus forms the lower part of the ankle joint by articulating with the tibia and fibula, and plays a key role in transferring body weight from

the leg to the foot. The calcaneus is the largest and strongest bone in the foot that lies inferior to the talus. The calcaneus transmits the majority of the body's weight from the talus to the ground when standing.

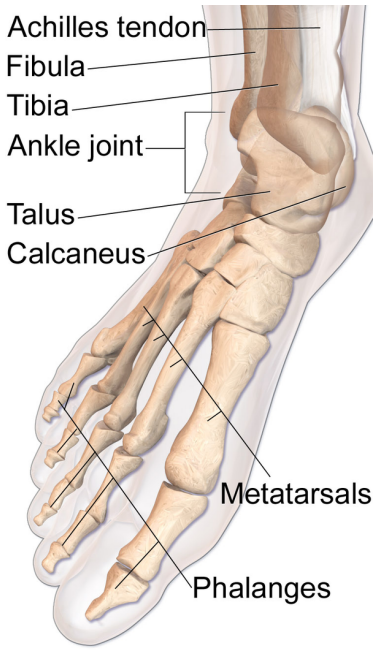


Figure 2.2: Bones of a Human Foot
(Adapted from [9])

The midfoot comprises five tarsal bones: the *navicular*, *cuboid*, and the three *cuneiforms* (medial, intermediate, and lateral). These bones are centrally located and articulate proximally with the hindfoot and distally with the forefoot. The navicular lies medially and articulates posteriorly with the talus and anteriorly with the three cuneiforms. The cuboid, positioned laterally, articulates with the calcaneus and provides structural support along the lateral aspect of the foot. The three cuneiforms are arranged in a row from medial to lateral and serve as keystone elements that contribute to the transverse structure of the foot.

The forefoot includes *metatarsus* and *phalanges*. The *metatarsus* consists of five *metatarsals* that are numbered one through five from the medial to the lateral side of the foot. Each metatarsal has a base proximally, a shaft, and a head distally. The base, which is broader than the distal end, articulates with the cuneiform and cuboid bones, forming the *tarsometatarsal* (TMT) joints. The heads are the main weight-bearing surface, and they

articulate with the proximal phalanges at the *metatarsal-phalangeal joint* (MTP), where the flexion-extension movement occurs. Large tuberosities created by the 1st and 5th metatarsals form a site for tendon attachment. The first metatarsal is notably shorter and more robust than the others, while the second metatarsal is typically the longest.

There are a total of 14 *phalanges*. The 1st digit (great toe) has 2 phalanges: proximal and distal. And the other four digits have 3 phalanges each: proximal, middle, and distal. Each phalanx has a base (proximally), a shaft, and a head (distally).

Additionally, the foot contains two small *sesamoid* bones embedded into a tendon beneath the first metatarsal on the bottom of the foot. These bones reduce pressure on the metatarsal head during walking and running. The foot's skeletal architecture is further supported by three primary arches: the medial longitudinal arch, which is high and resilient; the lateral longitudinal arch, which is lower and more rigid; and the transverse arch, which spans the midfoot. These arches collectively function to absorb impact, distribute loads, and maintain balance during dynamic activities.

The foot contains a complex network of ligaments that play a crucial role in maintaining stability, supporting arches, and facilitating movement. Key among these are the plantar ligaments, which include the long plantar ligament, short plantar (calcaneocuboid) ligament, and the plantar calcaneonavicular (spring) ligament, all of which support the longitudinal arch by resisting excessive flattening of the foot. Dorsal ligaments, such as the dorsal tarsometatarsal and interosseous ligaments, connect the tarsal and metatarsal bones and contribute to midfoot stability. The deltoid ligament on the medial side of the ankle provides strong support to the medial arch and resists eversion, while the lateral ligaments (including the anterior talofibular, calcaneofibular, and posterior talofibular ligaments) stabilize the ankle joint laterally and prevent excessive inversion. Collectively, these ligaments work in concert with muscles and bones to allow for dynamic motion while maintaining the structural integrity of the foot during weight-bearing activities.

Longitudinal Arches of the Foot

The arches of the foot consist of medial and lateral parts, which work together to act as shock absorbers, distributing weight over the foot, and as springboards for moving it during walking, running, or jumping. The medial longitudinal arch is higher and extends from the calcaneus to the first metatarsal, incorporating the talus, navicular, three cuneiforms, and the first three metatarsals. The talus is a key bone in this arch, serving as the main receiver of body weight from the tibia. The lateral longitudinal arch is lower and includes

the calcaneus, cuboid, and the fourth and fifth metatarsals. These bony structures form the foundation of the foot's arch system, enabling its mechanical function during locomotion.

The longitudinal arches distribute weight evenly between the heel and forefoot and help the foot adapt to uneven surfaces during gait, reducing mechanical stress. They also interact with the transverse arch to form a stable three-dimensional support. The medial arch is often described using two biomechanical models: the beam model and the truss model [10, 11] (Figure 2.3). In the beam model, the arch behaves like a curved beam with tensile forces on its lower surface and compressive forces on its upper surface, stabilized by joints and ligaments. The truss model describes it as a triangle, where bones act as struts under compression and the plantar fascia serves as a tie rod in tension. During weight bearing, the arch flattens slightly to absorb ground reaction forces (GRF), an important factor to consider in the design of anatomical foot forms.

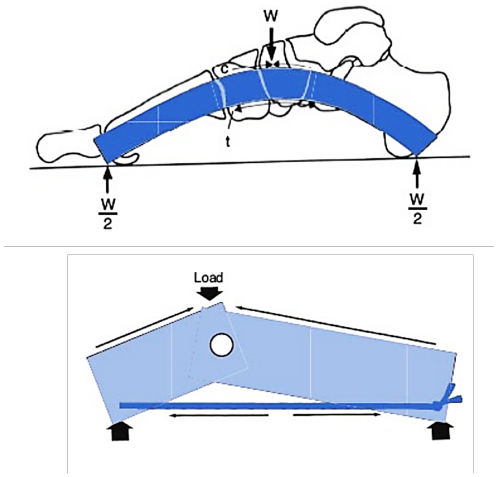


Figure 2.3: Medial Longitudinal Arch Models
(Adapted from [11])

2.2 Mechanical Behaviour of Metatarsals

The overarching theme of the current study is preventing injury to metatarsals by developing a better test method for safety footwear. Various studies, both experimental and computational, have investigated the mechanical and injury behaviour of metatarsals. Danesi et al. (2012) evaluated the strength and stiffness of individual human metatarsal bones and

found that the first metatarsal was significantly stiffer in all loading conditions compared to the others. Moreover, the study also discovered that the second metatarsal was less stiff than the third and fourth metatarsals under bending [12]. A study by Guntekunst et al. (2013) [13] investigated the strength of human metatarsals and found that mid-diaphysis bone thickness, buckling ratio, minimal moment of inertia, and minimal section modulus are the influencing factors to evaluate the strength and fracture risk of metatarsals. Kalra et al. (2021) [14] quasi-statically loaded cadaver feet on the dorsal side and developed an injury risk curve for metatarsals based on fracture force. Fung et al. (2017) [15] experimentally validated the FE model of human metatarsal bone for bone strain prediction and developed a relationship between density and modulus, which improved the accuracy of the FE Model. Fujikawa et al. (2017) [16] performed static fracture tests on ursine feet and developed a predicted fracture risk curve for human female metatarsal bones. Kalra et al. (2023) [17] performed impact tests on intact human cadaver feet and developed a metatarsal fracture risk curve based on impact energy and peak impact force.

2.3 Foot Injuries

Foot injuries are the most common type of emergent workplace injuries, which lead to significant disruption to an individual's quality of life and work productivity [18]. These injuries also frequently lead to extended periods of rehabilitation and recovery, with a possibility of inability of the employee to return to work [19]. According to the National Safety Council, during 2021-2022, there were 151,370 work-related foot injuries reported in the United States that resulted in work restrictions or employees being absent from the workplace [1]. Further insights from the National Trauma Data Bank for foot and ankle fractures indicate that the forefoot is particularly vulnerable, accounting for 18% of the total injuries [20].

Among these, fractures of the metatarsals represent 35 to 55% of all foot and ankle fractures [2, 3]. Metatarsal fractures typically arise from high-energy trauma such as direct impacts from falling objects, or accidents involving heavy machinery, all common in industrial settings [4]. These fractures can result from both acute high-force impacts and repetitive stress mechanisms, including overuse injuries in physically demanding work environments.

A study found that 58.4% of foot injuries happened due to being struck by an object, emphasizing the need for effective preventative strategies and protective equipment in workplace environments [18]. Protective equipment such as metatarsal guards has been developed to protect metatarsals from such injuries [21].

2.4 Metatarsal Guards

Metatarsal guards are common PPE used in safety footwear designed to shield the upper foot from impact injuries. A metatarsal guard spans the dorsum of the foot, extending from the toe cap to cover the metatarsal bones. These metatarsal guards can be added externally or integrated within the boot and provide protection. However, external guards perform better against stronger impacts [22]. Manufacturers have developed two main types of metatarsal guards: hard shell-like designs and soft foam designs. Hard metatarsal guards are generally plates or shells made of rigid materials like steel, aluminum alloy, or hard thermoplastic, which deflect and spread the impact forces [23]. Soft metatarsal guards are made of an absorptive material that is flexible at rest, but upon impact momentarily hardens or freezes to create a protective shield. These guards discreetly protect the metatarsals while offering greater flexibility and ergonomic comfort [24]. Current research has not explored whether hard metatarsal guards or soft metatarsal guards offer more protection. Figure 2.4 depicts the two different external metatarsal guard types.



(a) Hard metatarsal guard (b) Soft metatarsal guard

Figure 2.4: Different metatarsal guard types

SDOs such as ASTM International and CSA International have developed standards and testing methods to establish optimum performance criteria for metatarsal guards in industrial settings. The following section provides a more detailed review of these standards.

2.5 Review of Standards

PPE plays a critical role in minimizing workplace injuries and is mandated by law under the Occupational Health and Safety Act (OHSA) [25]. To maintain high safety standards and ensure consistent performance, several regulatory bodies have developed standardized testing protocols. This section provides an overview of four standards that evaluate the impact resistance of PPE, highlighting their criteria, testing methods, and relevance to occupational safety.

2.5.1 Protective Footwear Standards

Safety footwear is one of the main components of occupational PPE. They are designed according to safety standards, providing protection against impacts, crushing, sharp or pointed objects, falling heavy objects, slipping, temperature changes, wet environments, corrosive substances, and electrical hazards. A few features common to safety shoes are the toe cap, anti-penetration plate, and slip-resistant sole [26]. Metatarsal guards are another feature of footwear that offers protection to the metatarsals. ASTM and CSA have developed standards to measure the impact resistance of metatarsal guards, and these are discussed in the section ahead.

American Society for Testing and Materials (ASTM)

According to ASTM F2412-24 [5], the metatarsal guards are supposed to span partially over the toe cap and completely over the metatarsal bone area. The metatarsal impact resistance test method evaluates the effectiveness of metatarsal guards integrated in the safety footwear using wax feet, made of five parts paraffin wax and one part beeswax, as a foot surrogate. The deformation after the impact is calculated and analyzed to obtain the performance of the metatarsal guard protection offered by the footwear.

The test uses an apparatus that consists of a rigid frame, Figure 2.5, that allows the impactor to fall vertically in a repeatable direction. The impactor is a solid steel cylinder that is positioned perpendicular to the longitudinal plane of the heel/toe axis at the impact point. The impact point, 89 mm for men and 86 mm for women, is measured from the front point of the toe towards the heel of the footwear. Three-half pair specimens, including left and right footwear, are randomly selected for evaluation. The testing is performed at 22°C room temperature and 50% room humidity. For men, a size 9 shoe is selected, and for women, a size 8. The shoes are constrained at the base plate with a mounting device

such that the point of impact aligns with the impactor. The test starts by measuring the width, from the bottom of the wax foot to the top, at the impact point. The wax foot form is inserted inside the shoe, and a heel block is used to secure it in place. The impactor is dropped from a height that results in an impact velocity of 2.995 m/s and creates a simulated workplace impact energy of 101.75 J. After impact, the wax foot form is removed, and the distance from the lowest point of the impression made in the wax foot form to the bottom surface of the foot form is calculated. These results are tabulated to understand the performance of the metatarsal protection footwear. Energy is used as opposed to force because applied energy can be controlled by altering mass and height, and can be reproduced across laboratories.

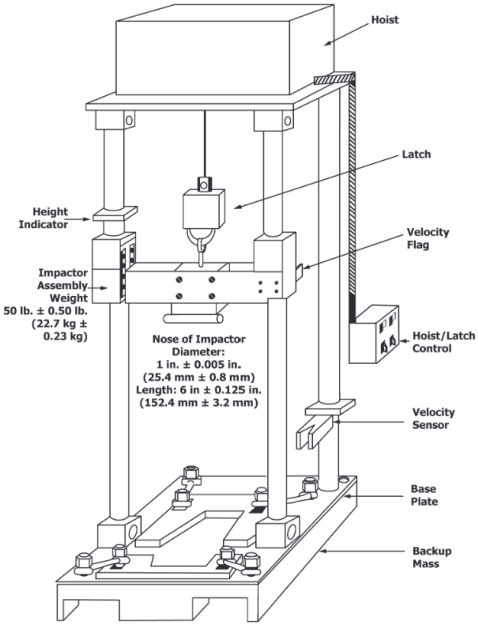


Figure 2.5: ASTM Metatarsal Footwear Impact Test Apparatus
(Adapted from [5])

Canadian Standards Association

CSA Z195:14 [6] states that the metatarsal protector should be of sufficient width and height such that it covers the complete dorsum of the foot. Moreover, the front of the metatarsal guard should overlap and rest on the protective toecap. A polyurethane-injected foot form is used as a foot surrogate with a cavity that is filled by a plasticine bar (25 mm

x 25 mm x 50 $\pm$ 2 mm) weighing 62 $\pm$ 3 g. The test apparatus is similar to the ASTM F2412-24 standard shown in Figure 2.5. The footwear is held in place at the heel on a heavy, rigid base having a thickness of at least 19 mm. The test begins by putting the polyurethane foot form with the plasticine bar inside the shoe, such that it aligns with the striker. The test begins by dropping the striker from a height such that the impact velocity is 2.99 m/s. After impact, the foot form is removed, and the height of the plasticine insert is measured. The deformation coined as internal metatarsal clearance is calculated to analyze the effectiveness of the metatarsal guard.

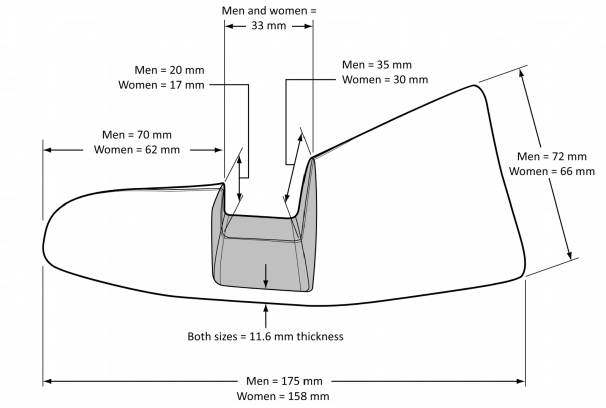


Figure 2.6: Foot Form Surrogate from CSA
(Adapted from [6])

2.6 Development of Human Body Surrogates

The development of human body surrogates plays a critical role in the evaluation of PPE to understand the injury mechanisms under controlled conditions [27]. In the domain of lower limbs, Klein [28] developed and validated a surrogate ankle for biomechanical testing. The study manufactured biofidelic skin to mimic soft tissue behaviour. Similarly, Chatterjee et al. (2024) [29] used 3D printing and 3D scanning techniques to create a human heel surrogate to assess slip risk. The surrogate was composed of a mixture of silicone of different shore hardness levels and was validated against the mechanical properties of a heel cadaver. Hrysomallis [30] developed a surrogate thigh model to test the protective performance of cricket thigh pads. The study used cadaveric data obtained through impact tests to find a soft tissue material that replicated the response. A stainless-steel beam was used to mimic the femur, and the model was instrumented with internal transducers to record peak forces.

In thermal studies, Demichelis [31] developed an additively manufactured foot manikin to determine thermal insulation provided by footwear (Figure 2.7b). The foot surrogate was embedded with temperature sensors, but encountered challenges with closed footwear. Unlike human feet that compress inside a shoe, the rigid geometry of the manikin it's compatible with standard footwear. Feeney [32] highlights that traditional footwear manufacturing often involves a U-throat design, which, when combined with safety toes, can lead to a bubbling effect in the forefoot, complicating fit for users. Upper-limb surrogate development for impact resistance has also seen advances. Alessa et al. (2023) [33] developed surrogate hand models for testing the impact resistance of gloves (Figure 2.7a). A composite hand surrogate fabricated out of 3D printing bone structures and synthetic gel to simulate tissue. The efficacy of gloves was tested through evaluation of both sensor-based force measurements and post-impact inspection for fractures in 3D printed bones.



(a) Surrogate Hand Model
(Adapted from [33])



(b) Foot Manikin
(Adapted from [31])

Figure 2.7: Examples of Surrogates

A recurring theme across these studies is the use of additive manufacturing techniques to iteratively refine anatomical surrogates. These techniques allow control over material properties and internal geometries. The next section talks about the theory of such design techniques within the domain of additive manufacturing.

2.7 Additive Manufacturing

Additive Manufacturing (AM) is a manufacturing technique that creates parts by adding material layer by layer. It provides design freedom, limits material wastage, and reduces lead time during the prototyping phase [34]. Because the material is added rather than subtracted, complex geometries can be manufactured with less effort. The general AM process is presented in Figure 2.8. It shows the process from digital design to layer-by-layer construction.

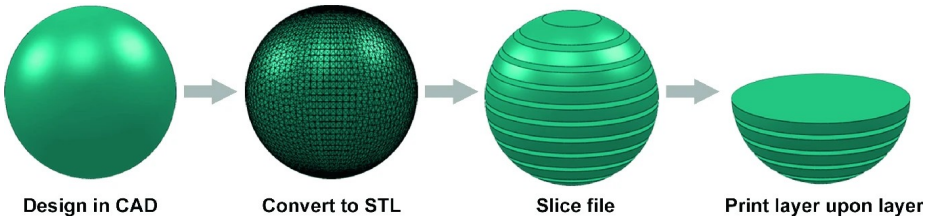


Figure 2.8: AM process chain
(Adapted from [35])

Several AM technologies have emerged that harness different energy sources like laser, electron beam, or ultrasonic vibrations [36]. In the following sections review two popular polymer-based AM technologies, stereolithography (SLA) and fused deposition modelling (FDM).

Stereolithography (SLA)

Stereolithography is a precise additive manufacturing technology that utilizes a photopolymerization process in which a liquid resin is selectively cured by a focused ultraviolet (UV) laser. The printing resolution is primarily determined by the diameter of the laser beam, which dictates the minimum feature size achievable in the fabricated part [37]. During the process, a laser beam is directed onto two mirror galvanometers that control its movement along the X and Y planes. These mirrors reflect and focus the laser beam upward through the build platform that is submerged in a vat of resin. The laser traces each cross-sectional layer of the part, solidifying the resin at targeted locations. After one layer is completed, the platform moves incrementally, and the next layer is cured on top of the previous one.

Fused Deposition Modelling (FDM)

Fused deposition modelling is a material extrusion-based additive manufacturing process in which a thermoplastic filament is heated to its melting point and extruded through a nozzle to form successive layers of the part [38]. The nozzle is moved along a predefined path, and each layer bonds to the one below as it cools and solidifies.

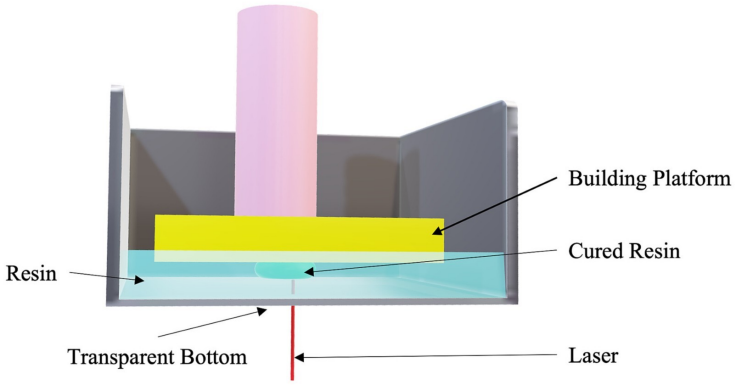


Figure 2.9: Schematic representation of SLA
(Adapted from [37])

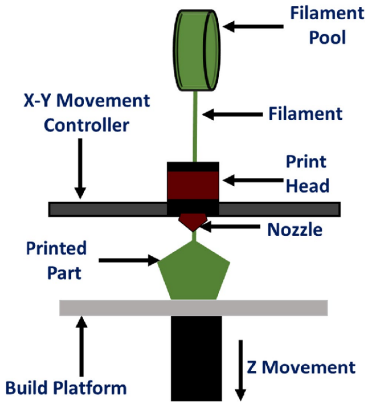


Figure 2.10: Schematic representation of FDM
(Adapted from [39])

Table 2.1: FDM vs. SLA: Advantages and Limitations

Technology	Advantages	Limitations
Fused Deposition Modelling (FDM)	• Relatively low cost • Wide material availability • Ease of use	• Lower resolution and surface finish than SLA • Anisotropic material properties
Stereolithography (SLA)	• High dimensional accuracy • Smooth surface finish • Intricate geometries	• Slower build speeds than some AM methods • Limited material selection • Requires post-processing (resin cleaning, UV curing)

2.8 Design for Additive Manufacturing

To fully leverage these benefits, engineers have developed Design for Additive Manufacturing (DfAM) frameworks [40, 41] and guidelines [42, 43] that help tailor designs to the strengths and limitations of AM technologies. Bikas et al. (2019) developed a framework that considers two main factors when designing for additive manufacturing: design aspects and design considerations [41]. A condensed version of the framework is shown in Figure 2.11. The optimization of both design aspects and design considerations leads to parts that are not only manufacturable but also meet quality and functional requirements.

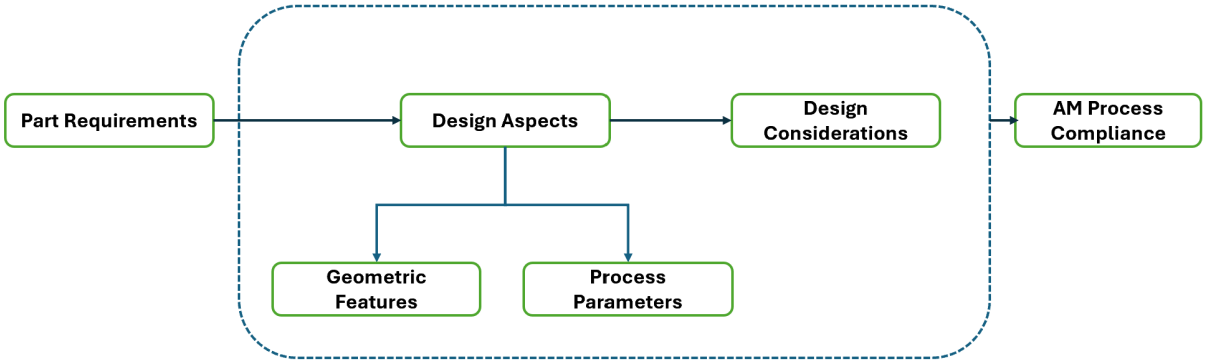


Figure 2.11: Design for AM Framework

2.8.1 Design Aspects

Design aspects in DfAM refer to specific features that can be adjusted or measured during the design and slicing stage. These include geometric features and process parameters used during fabrication. By understanding these aspects, designers can ensure the quality and accuracy of the part. Below, key geometric features and process parameters are outlined.

Geometric Features

Geometric features are specific shapes and characteristics of a 3D model that are defined by the types of AM technology being used. These include overhanging geometries, wall thickness, and feature sizes. Overhangs are surfaces that are insufficiently supported relative to the build vector and often require supports. For extrusion processes (FDM), support-free fabrication typically requires overhang angles (45°) [44], whereas inverted vat photopolymerization (SLA) can accommodate shallower overhangs (20°) due to resin support and upside-down building [45]. Minimum wall thickness is the smallest possible thickness a structure can have while maintaining functionality. It is defined by nozzle diameter, laser spot, and flow focal point. Walls below these thresholds may buckle or warp during cooldown [46], and excessive height-to-thickness ratios further elevate collapse risk [41]. The smallest detail that can be accurately reproduced is the minimum feature size. These are determined using benchmark artifacts across processes [47].

Process Parameters

Process parameters are selected during the slicing stage of the process and govern build quality, accuracy, and time. Parameters include layer thickness, build orientation, support structures, lattice, and infill density. Layer thickness refers to the thickness of each layer of material. It influences the quality as well as the build time of the part. An increase in layer thickness can increase the compressive strength of the part printed [48]. Build orientation refers to the positioning of the part concerning the print bed. It influences support structures required, tolerance errors, and anisotropy. Vertical build orientation compared to horizontal, increases the build time of printed parts [49, 50]. A few more process parameters relevant to the scope of the study are discussed briefly.

- **Support Structures**
  Support structures are temporarily printed alongside a part to provide stability to

prevent collapse during the printing process. These structures are viewed as important, although they have a few drawbacks. These structures increase material consumption, energy usage, manual post-processing and affects the surface quality[51]. Ideally, support structures should be eliminated, but in cases where it is not possible, optimization should be done to reduce the effect. Zhao et al. (2018) developed an inclined layer printing technique to eliminate the need for support structures when using FDM technology [52]. Furthermore, different additive manufacturing methods should have different design strategies for supports. In case of SLA, support volume and build time are key concerns, since the technology has high resolution, support removal from the area where it contacts has minimal effect on surface quality. For FDM, however, both the support contact area and build time are crucial [51].

- **Latticing**
  Latticing is the process of replacing solid volume in part with repeating internal structures called lattices. A lattice structure can be classified into ordered or stochastic cellular arrangements of unit cells [53]. A unit cell is the smallest element that makes up the whole lattice structure. The size of the strut of this unit cell is the smallest feature that needs to be printed by an AM technology. Therefore, the size of this unit cell is influenced by the minimum feature size that can be manufactured by the AM technology.

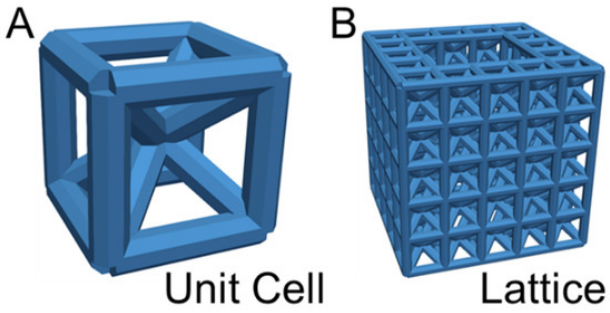


Figure 2.12: Difference between Unit Cell and Lattice
(Adapted from [54])

Selection of lattice structures is dependent on the material's mechanical properties, AM technology used, and porosity [55]. Some of the uses for lattice structures are light-weighting, energy absorption, and cost reduction. Ozdemir et al. (2016) [56] studied the energy absorption characteristics of cubic, diamond, and re-entrant lattice structures and found that cubic and diamond structures were able to distribute

the impact loading and reduce the peak impact stress overall. Jin et al. (2019) [57] investigated four different lattice designs computationally and observed that lattice structures with a stretching dominant deformation mode are more likely to exhibit better mechanical properties under dynamic loading. In a study by Egan et al. (2017), a computational approach was developed for modelling scaffolds with lattice structure, and topologies were tested using finite element analysis [58]. Extensive studies explore topology optimization techniques to achieve specified mechanical properties required [59].

- **Infill Density**
  In many AM processes (notably FDM), parts are not required to be printed solid. The interior can be filled with lattice structures discussed in previous sections. Infill Density refers to the fraction of interior volume that is solid material. A 20% infill density means 80% of the interior volume is air gaps. A study by Ambati suggests that tensile strength increases with an increase in infill density[60]. Another study by Nguyen et al. (2025), which evaluated cast moulds at different infill densities, suggested that there was a linear increase in nominal stress, but tensile strain varied [61]. Different lattice patterns with varying infill densities are illustrated in Figure 2.13.

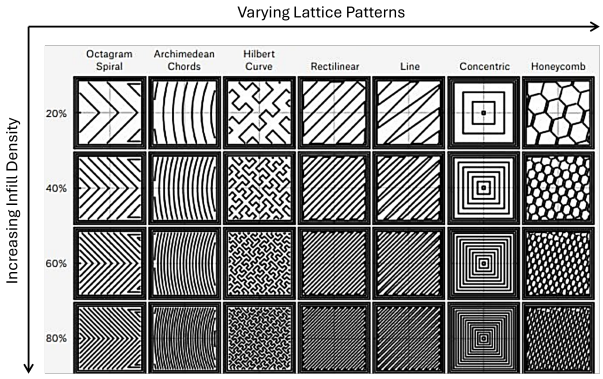


Figure 2.13: Lattice Patterns with increasing infill densities (Adapted [62])

All the design aspects affect the manufacturability of the part and consequently the design considerations as well. Therefore, it is important to list the design considerations before beginning the process of manufacturing.

2.8.2 Design Considerations

Design considerations are the results of the manufactured part. These can be the goal of the AM process. It includes specific mechanical properties, build time, and accuracy. Anisotropic mechanical properties behaviour is observed in 3D printed parts as they are built layer by layer. This difference in orientations can lead to differences in mechanical properties. With FDM, parts printed exhibit apparent anisotropy, which can be lowered by printing at a higher extrusion temperature. When printing with SLA, the parts are not entirely isotropic; however, the differences are minimal between part orientations [63]. When designing a model, it is essential to orient the part so that the loads applied are in the direction where mechanical strength is greatest.

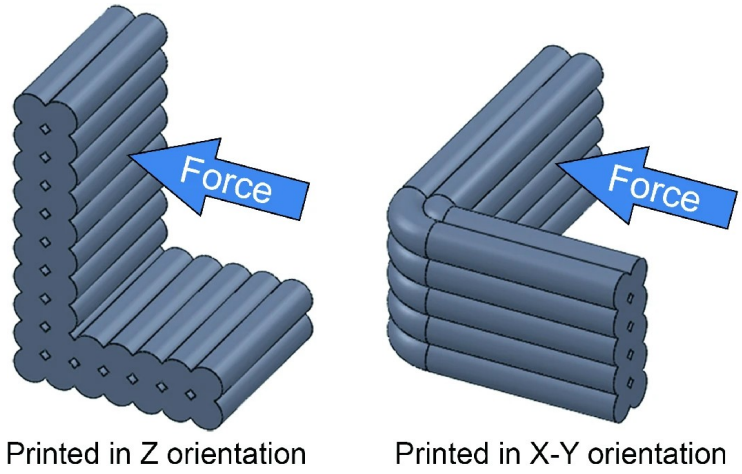


Figure 2.14: Effect of Build Orientation on Anisotropy
(Adapted from [64])

The accuracy of the machine in the xy axis and z axis is important to know before designing parts or different parts that would be connected. By having this understanding, appropriate tolerances can be applied to it. In the z-axis, the z-wobble effect is observed, and in the xy axis, filament inconsistencies are present [65].

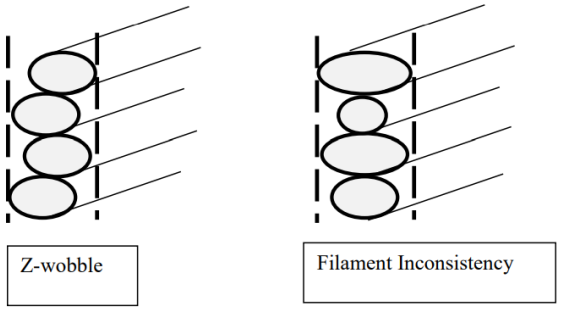


Figure 2.15: Accuracy in xy plane and z axis

Build time is the total time required for the AM part to be manufactured. Material deposition speeds on the xy plane and z axis vary, with the former being faster. Therefore, parts that are horizontally orientated are printed faster than vertically orientated ones [66]. More layers result in a longer build time.

By following DfAM guidelines, designers can confidently exploit additive manufacturing to create components with tailored mechanical properties. The following section discusses a few applications of these guidelines.

2.8.3 Applications of Design for Additive Manufacturing

Additive Manufacturing enables the production of complex three-dimensional geometries that are difficult or impossible to achieve with traditional manufacturing methods. In particular, lattice and cellular structures allow precise control over mechanical properties such as stiffness, energy absorption, and deformation behaviour. These capabilities make AM particularly attractive for creating lightweight, customizable components in sectors ranging from protective equipment and footwear to biomedical devices and automotive systems. Understanding how geometric design and process parameters affect the mechanical behaviour of these structures is a crucial first step before their deployment in practical applications.

Studies on 3D-Printed Lattice Structures

Before exploring applications, several studies have focused on understanding the mechanical behaviour of 3D-printed lattices. De La Rosa et al. (2021) [67] analyzed TPU lattices and

demonstrated that stiffness and compressive response are highly dependent on cell topology, lattice density, and orientation, providing methods to predict and optimize elastic behaviour for customizable products. Bates et al. (2019) [68] investigated density-graded TPU honeycombs, showing that grading can tailor energy absorption and damping while maintaining performance under cyclic and impact loading. Similarly, Habib et al. (2019) [69] numerically studied octagonal and Kelvin lattices, revealing that such designs can surpass traditional honeycombs in energy absorption when stress thresholds are carefully controlled. Nowak et al. (2024) [70] extended these concepts to layered engineering materials, developing a ULTEM-polycarbonate sandwich composite that balances cost and mechanical performance, highlighting AM's potential for customized structural components.

Applications of 3D-Printed Lattice Structures

Building on these fundamental studies, researchers have applied AM lattices to functional products across multiple sectors. Lee et al. (2019) [71] demonstrated that TPU lattices can be tuned for tensile strength and shock absorption, confirming their suitability for personal protective equipment such as pads and guards. In the footwear sector, Davia-Aracil et al. (2018) [72] highlighted that AM enables zonal control for cushioning and plantar pressure redistribution, while Jandová et al. (2022) [73] showed that fully customized 3D-printed insoles effectively reduce peak plantar pressure, particularly for high-arched feet.

Further advancing functional footwear, Zhang et al. (2024) [74] introduced auxetic lattice midsoles for diabetic patients, achieving up to 55% reduction in peak plantar pressure, while Tang et al. (2019) [75] designed functionally graded insoles that increased foot contact area by 30% and reduced peak pressure by 35%, demonstrating the ability of AM to deliver patient-specific biomechanical optimization. In biomedical devices, Badini et al. (2023) [76] applied 3D printing to create lattice-based hand-wrist orthoses for patients with motor neuron disease. Finite element analysis and patient feedback guided the design of form-fitting, biocompatible devices with tunable mechanical responses to support weakened muscles and improve functional outcomes. Finally, Niutta et al. (2022) [77] exemplify the extension of AM lattices to engineering applications, designing carbon nylon automotive crash absorbers with optimized unit cell geometry. These structures reduced mass by 25% and provided smoother force–displacement responses compared to steel components, illustrating AM's potential for lightweight, high-performance energy-absorbing applications.

2.9 Knowledge Gaps and Opportunities

AM enables designer control of internal architectures, supports, and infill to tailor a cadaver–like response. For metatarsal guard performance testing, this capability of AM is particularly useful: elastomeric, lattice-tuned surrogates can be fabricated to reproduce foot cadaveric behaviour while accommodating embedded sensors. Parametric studies generally vary infill density, unit cell size, and topology to balance stiffness, energy absorption, and mass. Within this context, an instrumented, AM-based foot surrogate offers a practical route to capture localized metatarsal-level forces under standardized impacts and to move beyond current testing methodologies.

After reviewing the relevant literature and standards for metatarsal guard testing, the following knowledge gaps and opportunities have been identified:

1. A biofidelic foot surrogate with embedded measurement capabilities that can be repeatedly used has not been explored yet for metatarsal impact resistance testing.
2. While altering process parameters is utilized in orthoses and other surrogates to match the force-deformation response, this methodology has not been applied yet to a foot model for standardized testing.
3. A force-sensor-based measurement system has not been applied to a foot surrogate to calculate transmitted force at the metatarsal location.

Chapter 3

Identification of a Biofidelic Foot Form Material

The goal of this chapter was to identify a material that mimics the cadaveric response obtained from literature. This material is then used to fabricate a biofidelic foot surrogate for evaluating the performance of metatarsal guards in protective footwear.

3.1 Evaluation Benchmark

To evaluate the biofidelity of the material, the force-deformation curve of the candidate material was compared with the cadaveric response under impact loading. The cadaveric reference data is obtained from a previous study by Kalra et al. (2023) [17]. The data was available at impact energies of 22, 33, and 44 J. However, for the scope of this study, an impact energy of 33 J was selected as it represents 50% fracture risk probability of the metatarsals, as reported by Kalra et al. (2023) [17]. The fracture probability curve for varying energies is shown in Figure 3.1.

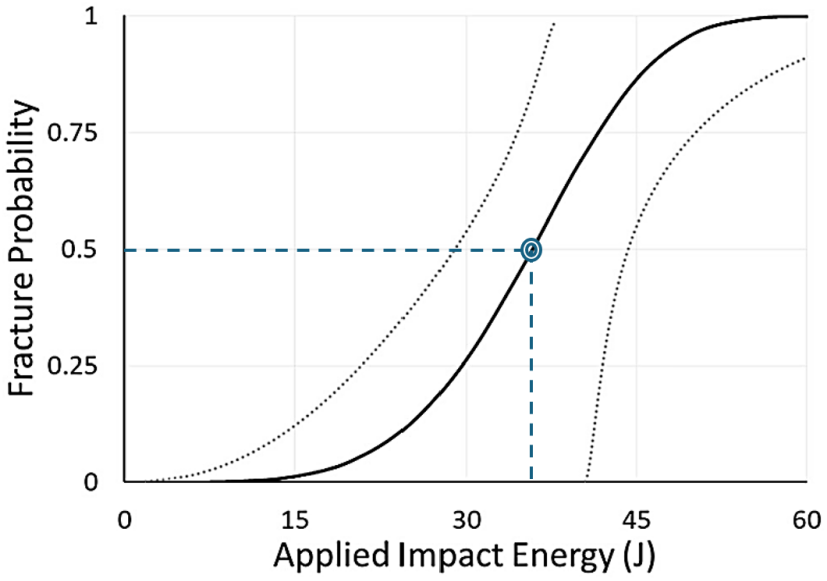


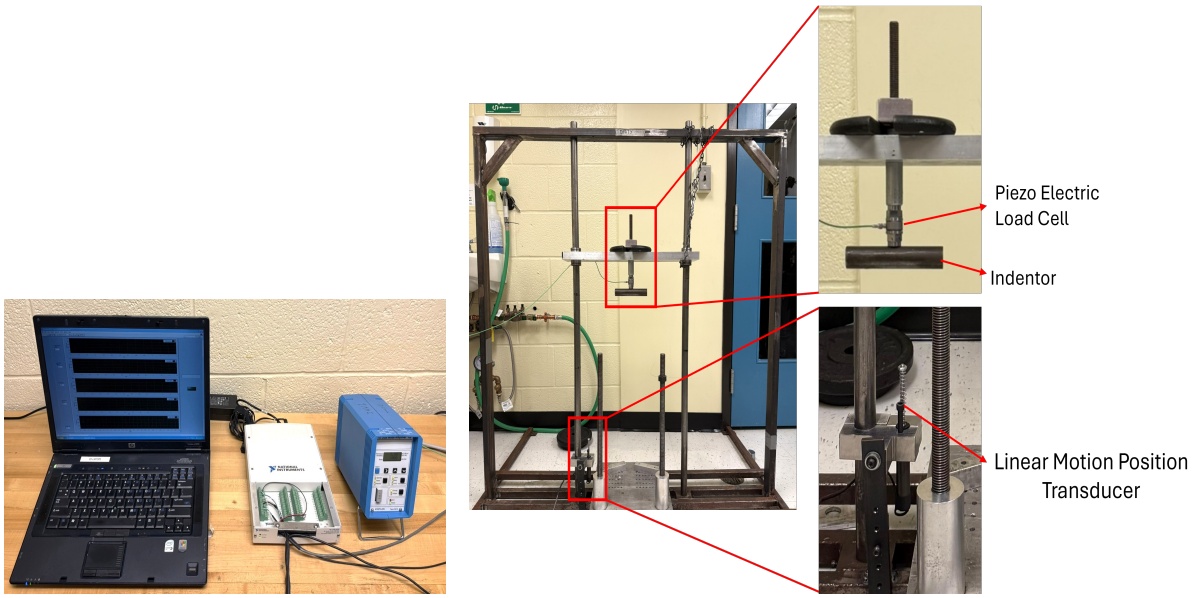
Figure 3.1: Fracture-risk curve of metatarsals based on impact energy
Adapted from [17]

3.2 Experimental Setup

The material selection methodology adopted in this study involves evaluating the force-deformation response of materials, obtained either through computational simulations or experimental testing. Simulation models are based on the experimental setup. For the experimental testing, a drop tower setup, analogous to ASTM test standards, is used. The impact tower comprises a flat base jig supported by an aluminum frame. A piezoelectric load cell is mounted between the indentor and a drop platform aligned with the impact axis to record transmitted impact forces. Impact energy is controlled by adding weights to this platform. A linear motion position transducer is affixed at the base to measure the vertical deformation of the specimen during impact. Force and displacement signals are recorded simultaneously. The key components of the setup are outlined in Table 3.1 and are shown in Figure 3.2b.

Table 3.1: Impact Tower Key Components and Specifications

Component	**Specification**
Piezo-Electric Load Cell	Kistler 9321B, 10 kN capacity, Kistler Instrument Corporation, Winterthur, Switzerland
Linear Motion Position Transducer	BEI Sensors 602R2KL.35, 50.8 mm travel, BEI Sensors, a Sensata company, Mansfield, Ohio, USA
Indentor	25.4 mm diameter, 127.0 mm length, steel
Data Acquisition System	National Instruments, Austin, TX



(a) (b)

Figure 3.2: (a) Data Acquisition System (b) Drop Tower Setup

The impact energies are calculated using the following equation:

$$E = mgh$$

where,

- E is the impact energy (J),
- m is the mass (kg),
- g is the gravitational acceleration (9.81 m/s^2),
- h is the drop height (m).

An impact energy of 33 J was achieved using a drop height of 0.5 m and a total mass (including the drop platform) of 6.2 kg. The following section focuses on developing a finite element (FE) model that mirrors these boundary and loading conditions to test for candidate materials.

3.3 Computational Pre-Screening

A computational modelling approach was used to pre-screen candidate materials and identify one whose force–deformation response under a 33 J impact falls within cadaveric corridors. An explicit-dynamics FE model was constructed using an ASTM-developed US men's size 9 foot model, together with a rigid base plate and an indenter arranged to reflect the drop tower setup. The boundary and loading conditions applied are analogous to the experimental setup. Candidate material models were parameterized from literature and utilized to generate force–deformation curves for comparison with cadaveric data. This simulation workflow reduces the need for manufacturing multiple foot forms with different materials by narrowing the material set to those most likely to meet the target response.

3.3.1 Development of FE Model

An ASTM-developed digital foot mesh (US men's size 9) was used. ASTM produced the model from a cast of a human foot, digitized it via 3D scanning, repaired and smoothed the mesh to reduce scan noise, and adjusted the geometry to align with mean anthropometric measurements for a size 9 men's foot. The acquired STL file was converted to 3D CAD in ANSYS SpaceClaim. An explicit dynamics study was then configured in ANSYS Workbench 2024 R1 to simulate impact tests under the same boundary and loading conditions as the experimental setup.

Setup and Boundary Conditions

The impact model consisted of three parts: a ground (rigid) plate, an indentor, and a foot model. The rigid plate is placed at the global origin, coinciding with its centroid. It is fixed in all degrees of freedom, and the foot model is placed on top of it such that the plantar side is in contact. The indentor followed the ASTM test-rig specification and was positioned approximately above the mid-metatarsal region on the dorsum of the foot. Figure 3.3 illustrates the setup of the FE model.

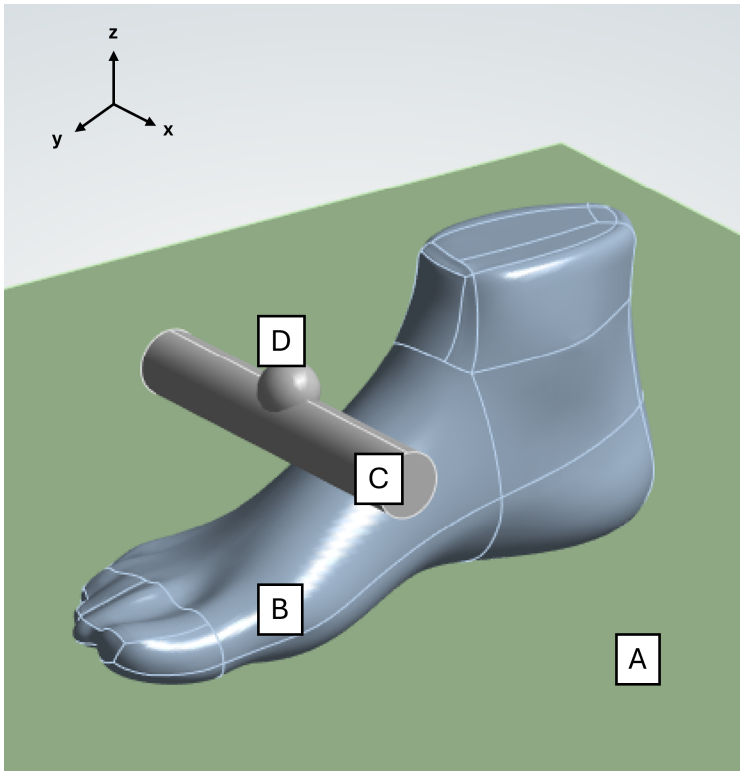


Figure 3.3: FE Model Setup: A-rigid plate, B-foot model, C-indentor, D-point mass (6.2kg)

To represent the drop assembly and deliver approximately 33J impact, a point mass, equal to the weight of the drop platform and an additional 2.2 kg weight, was added along the top of the indentor. The foot form is constrained by two fixed supports applied at a front vertex and a rear vertex. The indentor was constrained to translate along the z-axis. Frictional contact was established between the foot-plate and indentor-foot pairs. Instead of prescribing a drop height, the indenter is assigned a constant velocity of 3.13 m/s, which

is calculated using the equation:

$$v = \sqrt{2gh}$$

where $g = 9.81\,\mathrm{m/s^2}$ is gravitational acceleration and $h = 0.5\,\mathrm{m}$ is the drop height

This velocity corresponds to the impact velocity experienced by an object under free fall from a height of 0.5 m, which is identical to the impact testing conducted on cadavers at 33J energy. As cadavers demonstrate viscoelastic behaviour, which is rate-dependent, it is important to maintain the same velocity for testing candidate materials in this study.

Materials

Five materials were tested as part of the FE study. The material properties and material model for each material are summarized in Table 3.2

Table 3.2: Materials and their properties for FE Study

Material	**Material Model**	**Material Properties**
Butyl Rubber	Linear viscoelastic (Prony series)	[78]
Ninjaflex ®(TPU)	Hyperelastic (Ogden)	[79]
Silicone Rubber	Hyperelastic (Mooney-Rivlin, 2-parameter)	[80]
Neoprene Rubber	Hyperelastic (Mooney-Rivlin)	[81]
Vulcanised Rubber (8% sulphur)	Hyperelastic (Ogden, 3rd order)	[82]

Results

The simulations were allowed to run for 0.025 seconds, and contact force and deformation response at the point of impact were gathered for evaluation. Out of the five materials tested, 8% sulphur vulcanized rubber showed similar energy absorption, force, and deformation patterns as a cadaver foot under the same loading conditions, shown in Figure 3.4. These findings indicate that a foot form manufactured using the identified material can be used to develop a surrogate for impact resistance testing of protective footwear.

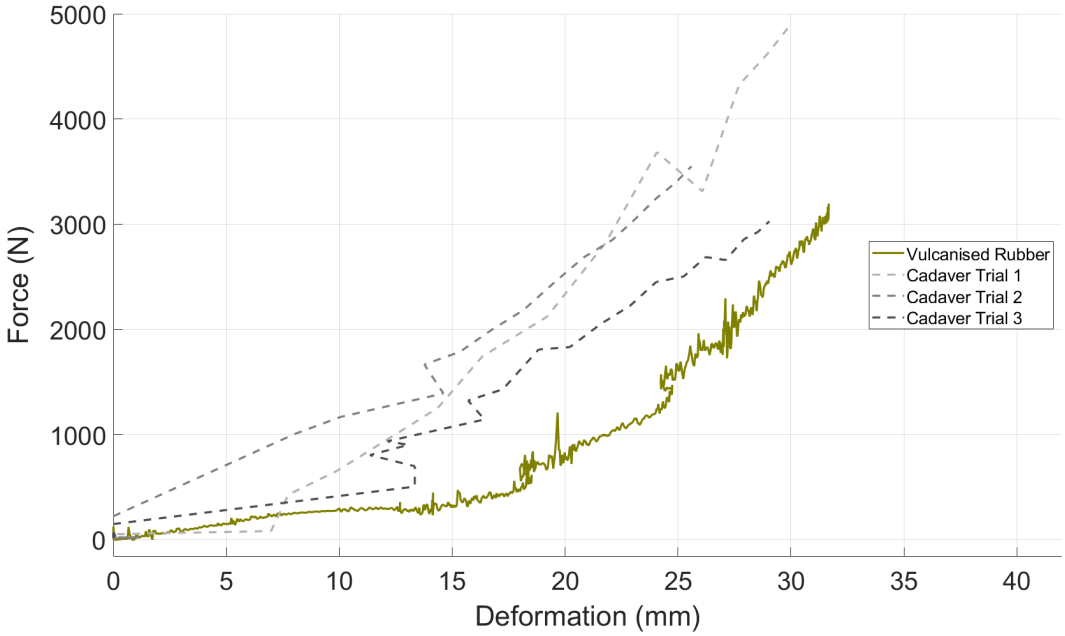


Figure 3.4: Force deformation response of vulcanized rubber vs cadaver at 33J impact energy

Although simulation results for 8% sulphur vulcanized rubber were favourable, fabricating a full foot form was not feasible within the project constraints. The material required custom material development and manufacturing, and no vendors were available to mould a complex foot geometry at a low volume. The quoted costs and lead times exceeded the experimental schedule. Therefore, commercially available rubber materials are considered for further experimental evaluation.

3.3.2 Experimental Verification of Alternate Rubber Material

The fabrication of a foot form using the identified material (8% sulphur–vulcanized rubber) was not practical within the established project constraints. Therefore, commercially available rubbers were used as an alternative. Two neoprene rubber blocks with Shore 50A and Shore 60A hardness were selected to approximate the stiffness of vulcanized rubber (Figure 3.5). Shore hardness was used only as a first screening criterion because it does not predict the rate and strain-dependent force–deformation response required for impact evaluation.

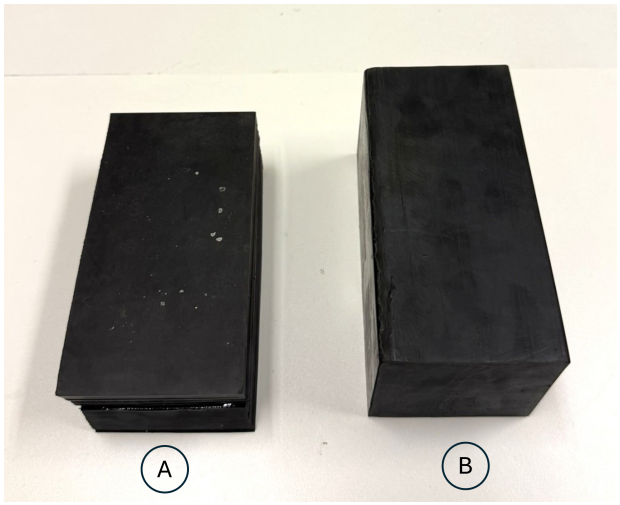


Figure 3.5: Rubber Blocks: A-Neoprene 60A , B-Neoprene 50A

Neoprene blocks were tested experimentally at a 33 J impact energy and compared to the responses obtained for the vulcanized rubber computationally with the same block geometries and under the same constraints. Two explicit-dynamics simulations were developed with an identical setup and boundary conditions. In place of the foot form, a rigid plate supported a cuboid matching each specimen: $2 \times 3 \times 6$ in for the 60A neoprene and $3 \times 3 \times 6$ in for the 50A neoprene. Each cuboid was assigned the constitutive properties of 8% sulphur–vulcanized rubber to produce target force–deformation curves for the same geometry and impact conditions. The comparison showed that neoprene rubber failed to reproduce a response that was comparable to the target force-deformation behaviour, indicating a mismatch in force, deformation, and energy absorption under impact.

Given the response mismatch and the constraints on fabricating a custom rubber foot form, the study adopted an additive manufacturing strategy. The next section details the additive manufacturing methodology to engineer a biofidelic material for the surrogate being developed.

3.4 Additive Manufacturing Approach

To implement the shift to additive manufacturing (AM), a design-optimization methodology was established to tune a material's mechanical response by altering process parameters

and geometry. Two 3D-printing technologies were used to fabricate the engineered materials. The following section details the AM methodology, including process parameter selection, manufacturing methods, and criteria used to assess biofidelity.

3.4.1 Fused Deposition Modelling (FDM)

Fused Deposition Modelling (FDM) was chosen first because it is a widely used additive manufacturing technique that can produce complex geometries with minimal material wastage and broad material availability. In the context of manufacturing, it serves a role similar to injection moulding [83]. The Prusa i3 MK3 (FDM) 3D printer was selected due to its performance, filament compatibility, and resolution to print this material.

In previous testing, 8% sulphur vulcanized rubber exhibited a force-deformation response closely resembling that of a human foot. On that basis, a hyperelastic material that can be additively manufactured and has similar energy absorption properties was optimum for use in a surrogate foot form. To meet this criterion, Ninjaflex ®, a flexible thermoplastic polyurethane (TPU) filament with a Shore hardness of 85A, was selected due to its rubber-like elasticity and capacity to undergo large reversible deformations.

The focus of this method was to optimize the additive manufacturing material, TPU, by altering its internal geometry. This was achieved by altering process parameters in the PrusaSlicer software. To tune the material stiffness and get the desired elasticity, two primary parameters were altered: lattice pattern and infill density.

To evaluate the effects of these parameters, foot sections were taken from the 3D foot model. The sections were selected based on the impact location, that is, the mid-metatarsal. Three sections were printed with a smaller length, and two foot forms were printed such that the plantar surface of the foot is included as well. Cubic and gyroid lattice patterns were selected based on their energy absorption capabilities [56, 84]. The lattice pattern and infill configurations of these sections are summarized in the Table 3.3, and shown in Figure 3.6

Table 3.3: Foot sections printed with TPU of varying infill densities and patterns

Part	**Lattice Pattern**	**Infill Density (%)**
A	Gyroid	30
B	Gyroid	40
C	Cubic	50
D	Cubic	60
E	Cubic	70

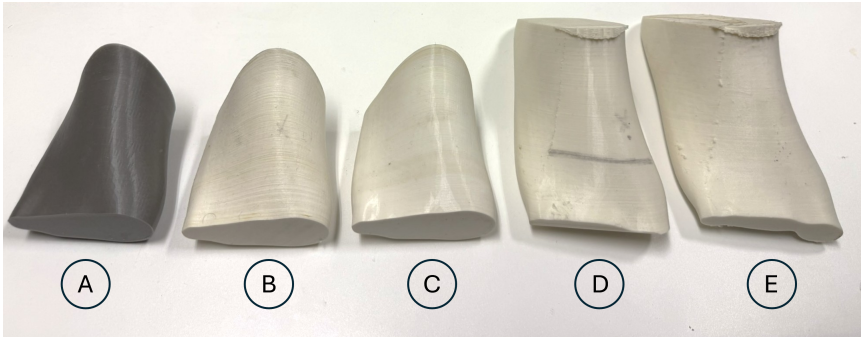


Figure 3.6: Latticed TPU sections

Printing flexible filament can be inherently difficult due to its low stiffness and high elasticity. Among the most critical factors that influence print quality are nozzle temperature, extrusion rate, and print speed. If the nozzle temperature is set too low or too high, the filament may bind and jam in the extruder. Excessive print speed prevents adequate filament deposition and cooling, producing weak, porous prints.

To overcome these issues, print parameters were optimized through trial and error using the slicing software. Final settings used are summarized in Table 3.4. Once these sections were printed, they were tested at 33J impact energy experimentally and assessed against the cadaveric benchmark.

Table 3.4: Optimum settings for 3D printing in PrusaSlicer with Ninjaflex ®

Setting	Value	Units
QUALITY		
Layer Height	0.2	mm
Initial Layer Height	0.02	mm
SHELL		
Wall Thickness	0.86	mm
Top/Bottom Thickness	1.20	mm
Top Layers	5	–
Bottom Layers	5	–
MATERIAL		
Printing Temperature	237	°C
Build Plate Temperature	60	°C
Flow	120	%
Enable Retraction	OFF	–
SPEED		
Print Speed	15	mm/s
Infill Speed	15	mm/s
Wall Speed	15	mm/s
Outer Wall Speed	15	mm/s
Inner Wall Speed	15	mm/s
Top/Bottom Speed	15	mm/s
Travel Speed	60	mm/s
COOLING		
Enable Print Cooling	ON	–
Regular Fan Speed	30	%

Results

It was observed that among all tested sections, the sample with a cubic lattice pattern and 70% infill density exhibited a force-deformation response closest to cadaveric data (Figure 3.7). It had similar forces and deformations under the same impact conditions.

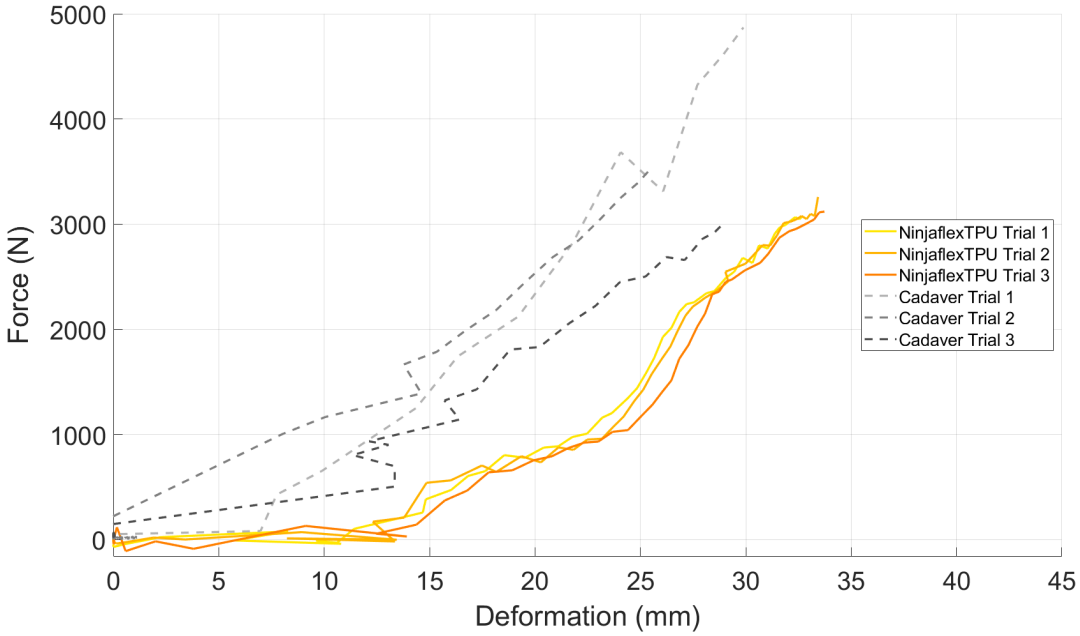


Figure 3.7: Force-deformation response of latticed Ninjaflex ® TPU vs cadaver at 33 J impact energy

Limitations

Despite successful prints, several limitations were observed during fabrication. Even after optimizing the settings, print times extended over multiple days, leading to issues such as layer shifting, nozzle clogging, and poor quality due to prolonged machine operation. Moreover, Ninjaflex ® TPU is highly sensitive to ambient humidity, and had to be completely dried in a dryer box before printing. During longer print times, the filament spool acquired moisture, which degraded the print quality. Due to persistent challenges, a decision was made to transition to an alternate additive manufacturing technology with better resolution, faster build time, and material stability.

3.4.2 Sterolithography (SLA)

The section examines the application of SLA-based 3D printing as an alternative to FDM to address the limitations encountered in previous fabrication attempts. A Formlabs 4

printer, which works based on the principle of SLA technology, is used for manufacturing samples. The section aims to identify and optimize an SLA-compatible material to replicate the impact response of the human foot obtained from a previous study.

Materials and Method

To identify a suitable alternative, printer-compatible resin options were evaluated, and Flexible 80A resin was selected. It was an optimum choice because its Shore hardness of 80A is close to Ninjaflex ® TPU 85A. In addition, it was developed to behave like rubber and TPU once cured, making it suitable for bending and compression applications. To minimize material consumption and ensure a valid comparison, a cuboid of dimensions 2 x 2 x 3 in made from Ninjaflex ® TPU with 70% infill density and a cubic lattice pattern is fabricated. Lattice structures were generated using nTopology software. Parameters varied in this process included: lattice type, infill density, and unit cell size. Unlike PrusaSlicer, nTopology does not automatically assign unit cell dimensions, so unit cell size was treated as an explicit design factor. These samples, along with the Ninjaflex ® sample, were impacted with 33J energy, and the force and deformation response were recorded for comparison between TPU and Flexible 80A resin samples. The specifications of latticed samples manufactured using Flexible 80A resin are provided in Table 3.5 and shown in Figure 3.8.

Table 3.5: Cuboids printed with Flexible 80A of varying infill densities, lattice patterns, and unit cell size

Part	**Lattice Pattern**	**Infill Density (%)**	**Unit Cell Size(mm)**
A	Truncated Cube	85	9 x 9 x 9
B	Cubic	70	6.35 x 6.35 x 6.35
C	Cubic	55	6.35 x 6.35 x 6.35

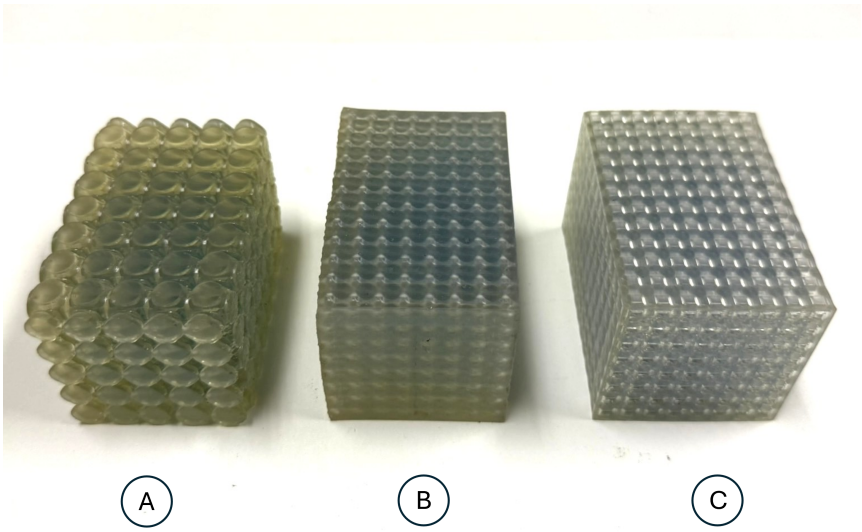


Figure 3.8: Resin latticed parts: A-truncated cube 80%, B-cubic lattice 70% and C - 55% cubic lattice

Results

The sample part with 55% infill density and simple cubic lattice pattern and unit cell size, 6.35 x 6.35 x 6.35 mm, exhibits a force-deformation response closely matching Ninjaflex ® TPU 70% infill density cubic lattice pattern, as shown in Figure 3.9. This makes it a viable substitute for Ninjaflex ® TPU. Periodic noise is observed in the graph, potentially because of electrical noise. This is expected as no digital filter was applied to the force-deformation data. SLA-printed parts also demonstrated high print quality with smooth surface finish and dimensional accuracy. Additionally, the build times were significantly lower compared to FDM, with each part completed in a couple of hours, including post-processing.

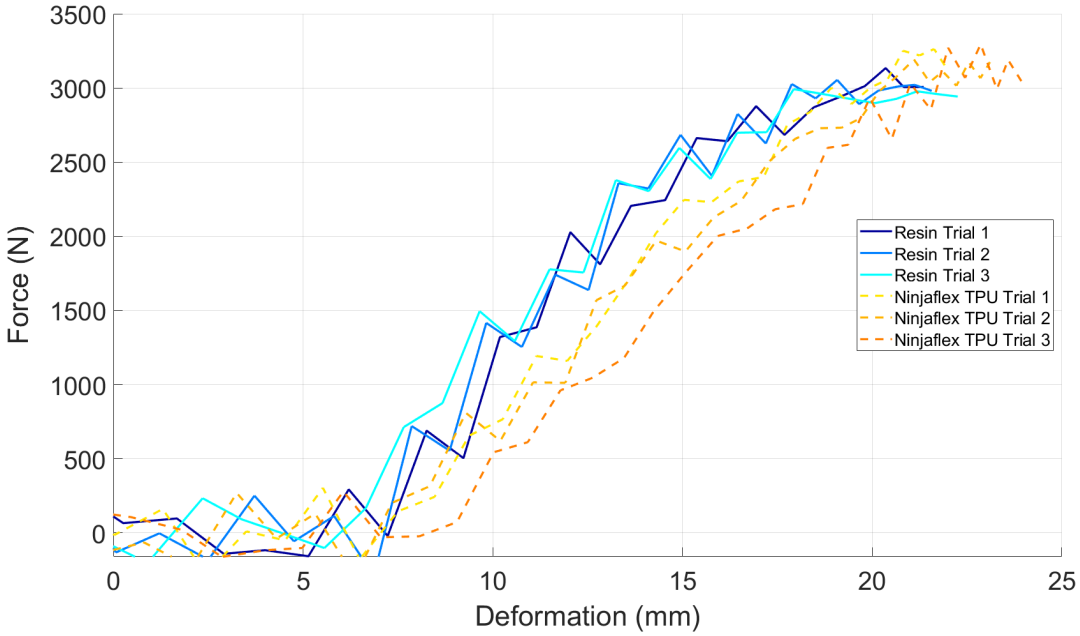


Figure 3.9: Force-deformation response of latticed flexible 80A resin vs latticed Ninjaflex ® TPU at 33 J impact energy

3.5 Chapter Summary

The purpose of this chapter was to identify and validate a material capable of showing biofidelic behaviour. Cadaveric force–deformation behaviour under a 33J impact was used as an evaluation benchmark. To gather data, a combination of computational and experimental methodologies was utilized. An ASTM analogous drop-tower was used to capture the force-deformation response experimentally, and FE models were developed using ANSYS Workbench 2024 R1. The results obtained from these methods established that 8% sulphur–vulcanized rubber most closely matched cadaveric behaviour in simulation. However, custom rubber manufacturing and low-volume moulding were not feasible within the project constraints, and commercially available neoprene rubber blocks did not reproduce the target response.

In response to these findings and constraints, an additive manufacturing pathway was adopted to engineer effective stiffness via lattice architecture and process parameters. Among printed candidates, an SLA Flexible 80A cubic lattice (55% infill; 6.35 mm cubic

unit cell size) reproduced the TPU benchmark response while improving manufacturability (shorter build times, higher surface quality, dimensional fidelity). The next chapter applies the selected SLA lattice configuration to the design, fabrication, and evaluation of a biofidelic instrumented foot form for the testing of metatarsal impact resistance offered by protective footwear.

Chapter 4

Design of Instrumented Foot Form for Force Measurement

This chapter presents the design framework used in the development of an engineered instrumented foot form for force measurement during metatarsal impact testing. Three prototype iterations of the foot forms were developed and tested, and the results of those are presented and compared.

4.1 Design Framework

This research adopts a systematic engineering design methodology developed by Pahl et al. (2007) [85], which offers a structured, engineering-focused approach to product development. The model has a logical progression from problem understanding to a validated solution as illustrated in Figure 4.1. The model is organized into four phases: *Planning and Clarifying the Task*, *Conceptual Design*, *Embodiment Design*, and *Detail Design*.

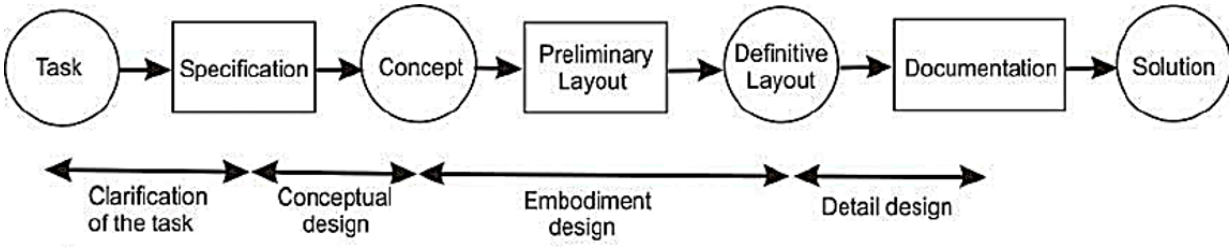


Figure 4.1: Design Framework Methodology
(Adapted from [86])

In the first phase, the design task is defined by understanding the problem from the user's perspective, which is further translated into design specifications. The conceptual design phase focuses on exploring and generating solutions based on requirements. All concepts are weighed against performance, feasibility, and user-related criteria. Promising concepts are selected for further development. During the embodiment design phase, the selected concepts are developed and tested against critical design requirements. The final phase, detail design, involves refining the design with the outcome being a complete solution. Throughout all phases, iteration and continuous refinement are encouraged as feedback ensures that the final solution is technically sound and aligns with user needs. Guided by this framework, the present study evaluates three application-specific prototypes.

4.2 Design Requirements

The design requirements derive from the study's initial objectives and specify a biofidelic, instrumented foot form that produces accurate, repeatable force measurements, is modular for repair and replacement, and remains durable under high-energy impacts. These requirements are listed in Table 4.1.

Table 4.1: Design Requirements for the Instrumented Foot Form

Category	Design Requirement	Rationale
Functional	Replicate the force-deformation response of cadaver feet under 33J impact.	Mimics real human foot behaviour for valid metatarsal guard testing.
	Support embedded force measurement at the metatarsal region.	Enables direct force measurement at risk-prone locations.
Mechanical	Deform elastically and return to their original shape.	Ensures reusability.
	Securely hold the load cell with accurate alignment.	Prevents partial readings.
	Withstand at least 100 repeated impact trials.	Ensures durability.
Material	Maintain dimensional accuracy and surface quality.	Ensures fit and performance in the test setup.
Manufacturability	Manufacture within 12 hours.	Supports rapid fabrication.
	Modular and repairable construction.	Enables easy replacement and maintenance.

4.3 Prototype I

4.3.1 Conceptual Design

The design of Prototype I was guided by several design requirements listed in the preceding section. A 3D model of a US men's size 9 foot was acquired from ASTM, providing a realistic anatomical geometry that can be used to develop a foot surrogate. To support modularity and reduce production costs, this prototype was fabricated using a combination of Flexible 80A resin and Polylactic Acid (PLA) filament. The primary material for the foot form was chosen as Flexible 80A, as established previously in Chapter 3. PLA was chosen for non-load-bearing structural components that support other parts of the foot form. It is a rigid and cost-effective material that can be quickly reprinted in case of failure. The assembled foot form is illustrated in Figure 4.2.

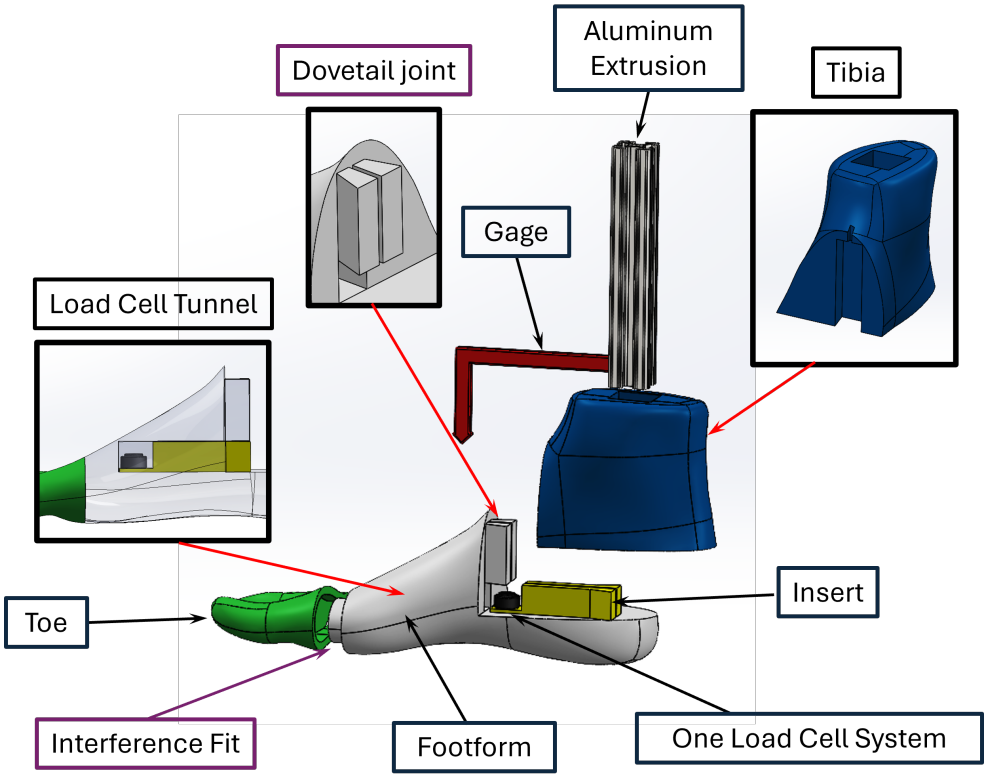


Figure 4.2: Concept Design of Prototype I

A load cell was embedded in the mid-metatarsal region. This ensures that impact forces are captured accurately and consistently during testing performed directly on the foot form or inside the boot. The load cell (DTB-2K Miniature Compression Load Cell, 2000 lbs capacity, Load Cell Central) was selected for its compact form factor and sufficiently high force capacity to withstand impact energies up to 33J. To secure this sensor, an insert was designed to place the load cell at the appropriate location, minimizing horizontal movements during impact. Moreover, a through gap is provided in the insert, allowing sensor wires to exit the structure without risk of damage.

The tibia and foot form body were connected using a dovetail joint with an intentional central gap to allow safe wire routing. The toe and foot form sections were joined using an interference fit, ensuring alignment and mechanical continuity during impact testing. The individual components of the foot form are detailed in Table 4.2. The manufacturability will be discussed in the next section.

4.3.2 Manufacturability of Prototype I

Prototype I is illustrated in Figure 4.3. Process parameters were tailored to the manufacturing technology. For stereolithography (SLA), parts were tilted by approximately 20° about the principal axes relative to the build platform to aid resin drainage and place supports on noncritical surfaces. Moreover, since SLA requires drain holes for resin drainage, certain faces of the lattice were strategically selected and generated without a boundary. A layer thickness of 0.1 mm was chosen. Parts manufactured through SLA require post-processing, and those requirements are different depending on the material. For Flexible 80A, the parts are washed in two cycles in isopropyl alcohol (IPA) twice (10 min per cycle) and then cured at 60° for 10 min.

For fused deposition modelling (FDM), parts were oriented flat on the build plate to minimize or eliminate the need for support structures, and printed with a layer height of 0.2 mm, thereby improving both surface finish and dimensional accuracy. A gyroid lattice was chosen for all parts as it is easy to manufacture. Table 4.2 summarizes the manufacturing specifications and estimated print time of each component.



Figure 4.3: Prototype I

Table 4.2: Manufacturing Specifications - Prototype I

Component	**Technology Used**	**Material**	**Latticing Parameters**	**Time (hrs)**
Load Cell	Commercial Sensor	Stainless Steel	N/A	N/A
Foot Form	SLA (Formlabs 4)	Flexible 80A Resin	Cubic, 55%, 6.35 mm	10
Toes	FDM (Prusa i3 MK3)	PLA Filament	Gyroid, 10%	0.5
Tibia	FDM (Prusa i3 MK3)	PLA Filament	Gyroid, 10%	1
Extrusion	Mechanical Component	Aluminium	Solid	N/A
Insert	SLA (Formlabs 4)	Resin / PLA	Solid	1
Gage	FDM (Prusa i3 MK3)	PLA Filament	Gyroid, 10%	0.5

When manufactured in parallel, the total production time is approximately 10 hours, including post-processing and support removal processes. This quick fabrication aligns with one of our design requirements, rapid manufacturability. Load cell and extrusion are two components that are procured from external suppliers and are not manufactured in-house. Therefore, depending on lead times, procurement can add to the estimated time needed to obtain a finished product.

Additionally, the cost of the data acquisition system is not included in the breakdown, as the current data acquisition system used is a high-end, research-grade unit from National Instruments, used along with LabVIEW software. For industrial deployment, a cost-effective alternative such as an Arduino-based system can be employed to interface with the load cell for real-time data acquisition. Figure 4.4 demonstrates how to place the Prototype inside the boot for drop tests.



Figure 4.4: Procedure to place the Prototype I inside the boot for testing

4.3.3 Experimental Testing

Prototype I is subjected to two rounds of testing. The first round was conducted to assess the biofidelity of the foot form, and the second round aimed to establish the benchmark for metatarsal guard impact resistance testing.

Biofidelity

To evaluate the biofidelity of the engineered foot form, impact testing was conducted at an energy level of 33J, consistent with conditions published in a previous study. The foot form was impacted as a complete assembly, and the resulting forces were recorded using the piezoelectric impact load cell. The results provide a basis for validating the foot form design as a suitable surrogate for wax during metatarsal protection testing under ASTM Standards. Figure 4.5 shows the response of the foot form compared to the cadaver foot.

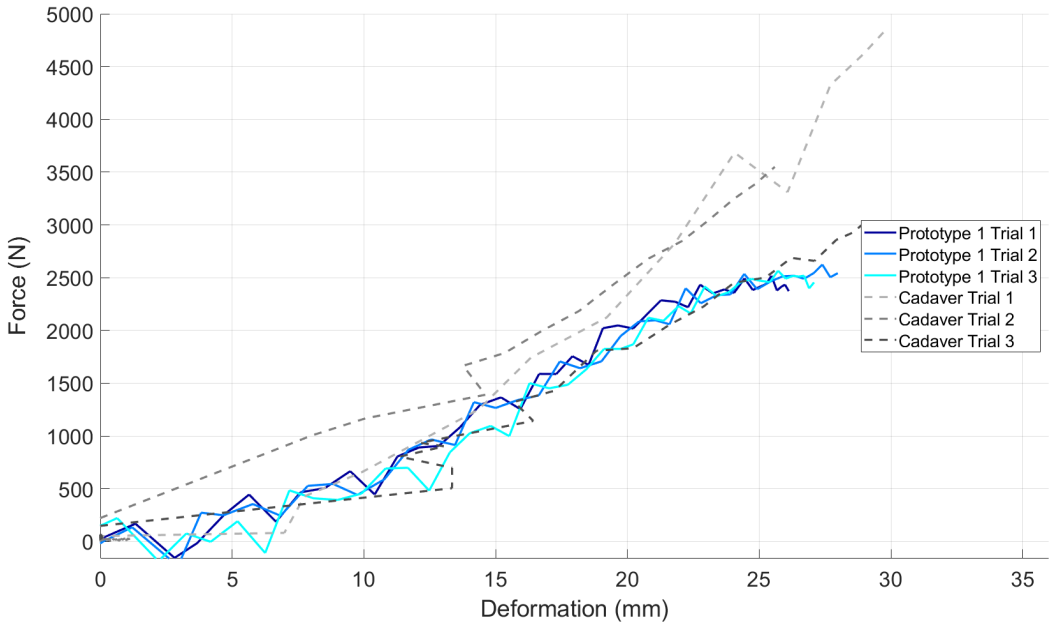


Figure 4.5: Force-deformation response of Prototype I vs Cadaver at 33 J impact energy

Benchmark

Based on the metatarsal injury risk curve presented in Figure 4.6, 20J impact energy corresponds to 10% risk of fracture. This threshold serves as a functional benchmark for evaluating protective performance. To test this benchmark, the foot form was subjected to five impact trials at 20J, and the embedded load cell response was captured and tabulated in Table 4.3.

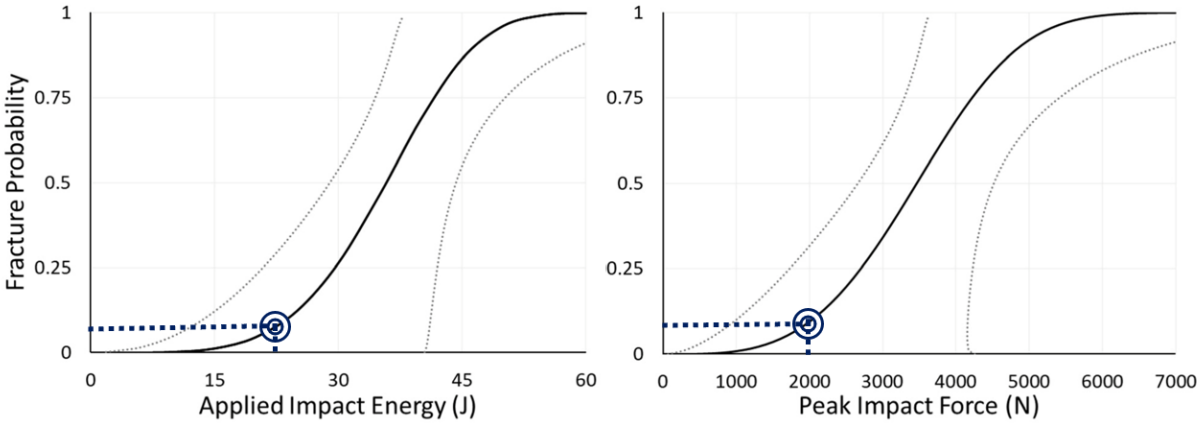


Figure 4.6: Metatarsal injury risk curves based on applied impact energy and force (Adapted from [17])

Table 4.3: Benchmark Testing for Prototype I

Trials	**Load (N)**	
	Load Cell	**Impact Load Cell**
1	270.81	1881.84
2	468.46	1926.90
3	211.94	1801.11
4	578.68	1978.13
5	515.78	1984.94
6	550.11	1971.97

4.3.4 Limitations of Prototype I

Prototype I demonstrated a biofidelic response when compared with cadaveric data at the same energy. However, it was observed during benchmark testing, the load cell response was variable, which suggested that testing with the surrogate in the boots would result in inconsistent results. Therefore, further testing was not performed. Although Prototype I

had a few advantages, there were a few limitations which prompted further development of the foot form.

1. The load sensing area of the embedded load cell was 11.5mm, which is very small (Figure 4.7). Consequently, a portion of the applied force during impact was not captured by the load cell as reflected in the results presented in Table 4.3.

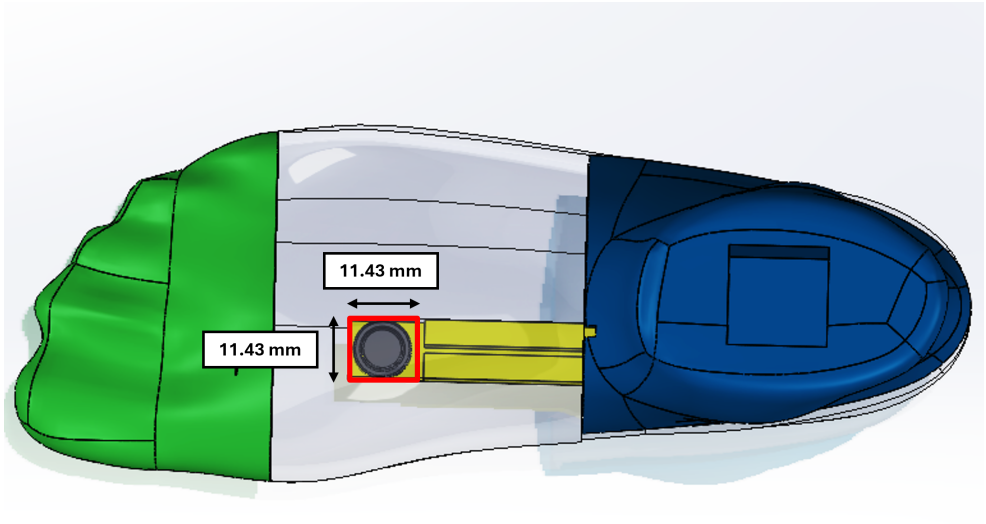


Figure 4.7: Load sensing area of a single load cell system

2. The foot form was initially developed without accounting for weight-bearing conditions. While the material of Prototype I had some flexibility, it did not have enough to conform to the internal structure of the footwear. Therefore, it was difficult to insert and remove it from the boot.

3. During impact, as the foot form would deform, the tibia component would shift upwards. This can be attributed to the dovetail joint being oriented at an angle relative to the impact axis during the drop test.

4.4 Prototype II

The design of the second prototype was led by the initial design requirements and the limitations observed in Prototype I.

4.4.1 Two Load Cell System and Validation

One of the limitations in Prototype I was the small force capture area of the embedded load cell. To overcome this, a two-load cell force measurement system was developed, as shown in Figure 4.8. Two load cells are mounted on a custom rigid stainless steel plate with an upper plate placed on top. The upper plate distributes the force among the two load cells depending on where the plate is impacted. Two posts prevent the movement of the upper plate relative to the bottom plate. For Prototype II, two load cells, each having a capacity of 1063.88 N, were procured. The specifications are provided in Table 4.5.

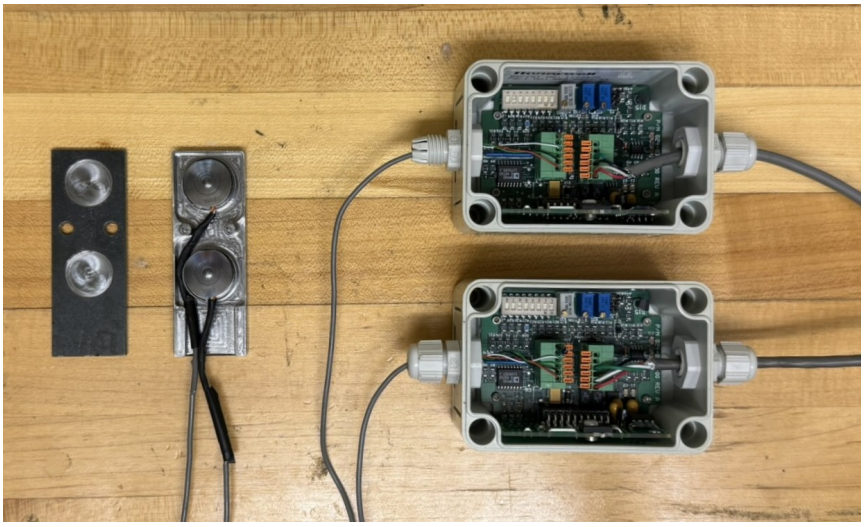


Figure 4.8: Two Load Cell System

A two-load cell system was validated by enclosing the load cells in a cuboid ($2 \times 3 \times 2$ in) made of Flexible 80A resin. The cuboid was manufactured using the same lattice parameters as the foot form. The test part was subjected to a 10J force at three different points. Points I, II, and III in Figure 4.9 show the three impact points along the top surface equidistant from each other.

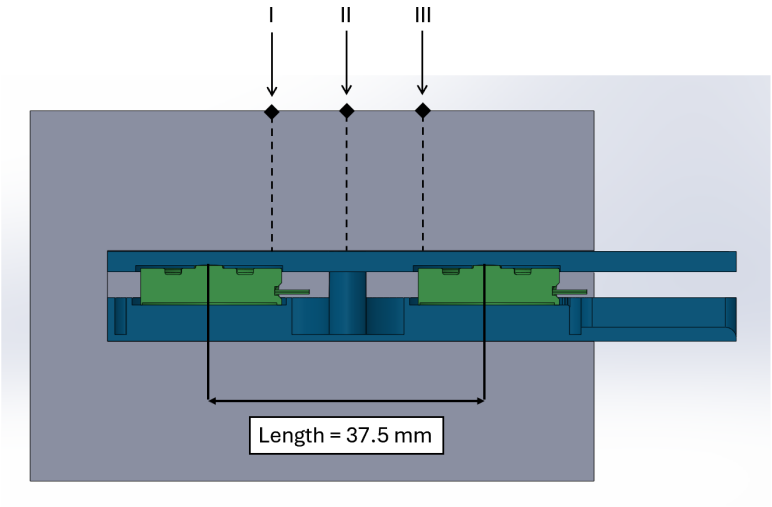


Figure 4.9: Section View of Load Cell Validation Setup

Table 4.4: Two Load Cell Validation Results at Three Different Impact Points

Impact Point	**Trials**	**Load (N)**			
		Load Cells		**Total**	**Impact**
		A	**B**	**A+B**	**Load Cell**
I	i	889.19	142.93	1032.12	1854.61
	ii	872.07	206.63	1078.70	1839.69
	iii	885.04	213.50	1098.54	1906.48
II	i	635.23	433.74	1068.97	1948.63
	ii	644.99	409.91	1054.90	1993.69
	iii	655.11	368.18	1023.29	1857.52
III	i	359.49	685.52	1045.01	1974.89
	ii	406.89	627.97	1034.86	1954.79
	iii	417.07	641.07	1058.14	1913.29

The validation results suggest that the total force read by the load cells stays consistent when impacted at 10 J energy across three different points. Therefore, the two load cell designs should give a consistent response when impacted anywhere within the 37.5 mm span between the two load cells.

4.4.2 Conceptual Design

Similar to the previous design, Flexible 80A resin was used for fabricating load-bearing components, and PLA was used for manufacturing non-load-bearing parts. The load cell tunnel was also redesigned and moved forward to allow for an even distribution of load between two load cells when impacted. To accommodate the tunnel shift, the tibia component was split into two components and joined using a dovetail joint. These parts were bottom-constrained rather than side-constrained to improve structural stability during impact. Prototype I encountered fitting issues within the boot; therefore, the model was scaled to $1 : 0.9 : 1$ in the x, y, and z axes, respectively, reducing the overall width. Lastly, the extrusion component previously purchased was replaced with a custom-manufactured version. This helped reduce the overall weight of the foot form and facilitated easy replacement in case of mechanical failure. The assembled foot form is illustrated in the Figure 4.10, and individual components are detailed in the Table 4.5

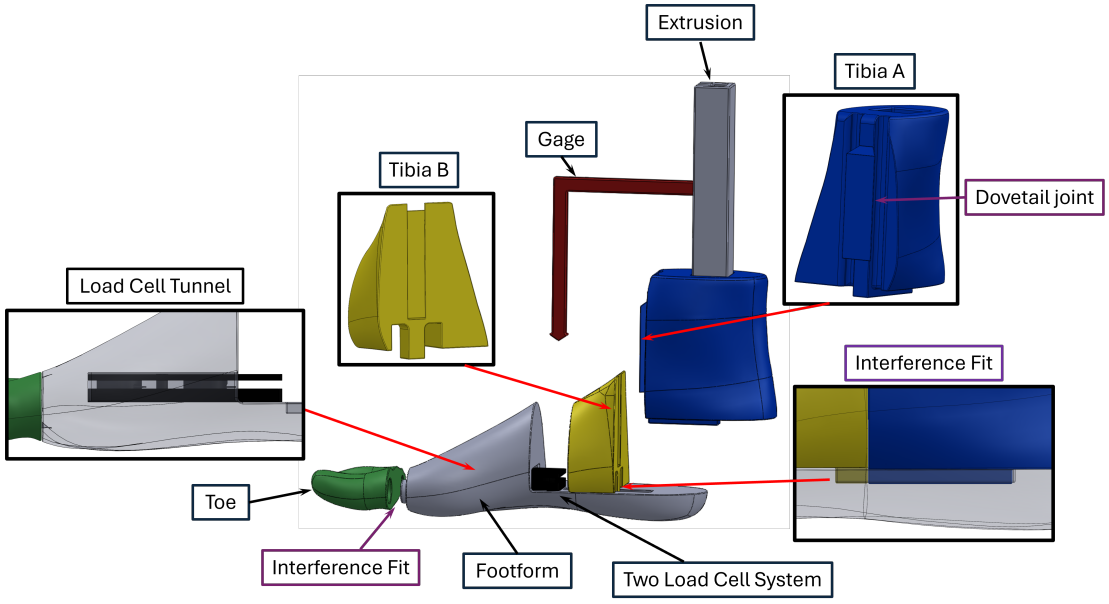


Figure 4.10: Concept Design of Prototype II

4.4.3 Manufacturability of Prototype II

Prototype II (Figure 4.11) was printed using the same additive manufacturing process parameters as Prototype I. The total time to manufacture Prototype II would be 9 hours, including post-processing if printed in parallel. Table 4.5 summarizes the manufacturing specifications and estimated print time of each component.



Figure 4.11: Prototype II

Table 4.5: Manufacturing Specifications - Prototype II

Component	**Technology Used**	**Material**	**Latticing Parameters**	**Time (hrs)**
Load Cells	Commercial Sensor	Stainless Steel	N/A	N/A
Foot Form	SLA (Formlabs 4)	Flexible 80A Resin	Cubic, 55%, 6.35	9
Toes	FDM (Prusa i3 MK3)	PLA Filament	Gyroid, 10%	1.5
Tibia A	FDM (Prusa i3 MK3)	PLA Filament	Gyroid, 10%	7
Tibia B	FDM (Prusa i3 MK3)	PLA Filament	Gyroid, 10%	2
Extrusion	FDM (Prusa i3 MK3)	PLA Filament	Gyroid, 10%	3
Load Cell Plates	Custom Manufactured	Stainless Steel	Solid	N/A
Gage	FDM (Prusa i3 MK3)	PLA Filament	Gyroid, 10%	1

4.4.4 Experimental Testing

Prototype II is subjected to multiple phases of testing. The first phase was comparing the mechanical response of Prototype II to cadaveric data to assess its biofidelity. This was followed by the response of embedded load cells subjected to three different impact energies. Lastly, a benchmark was established, and the foot form was tested in three different types of safety boots to validate its performance across different protective footwear configurations.

Biofidelity

Figure 4.12 shows the force-deformation behaviour of foot form Prototype II compared to cadaver feet under 33J impact energy.

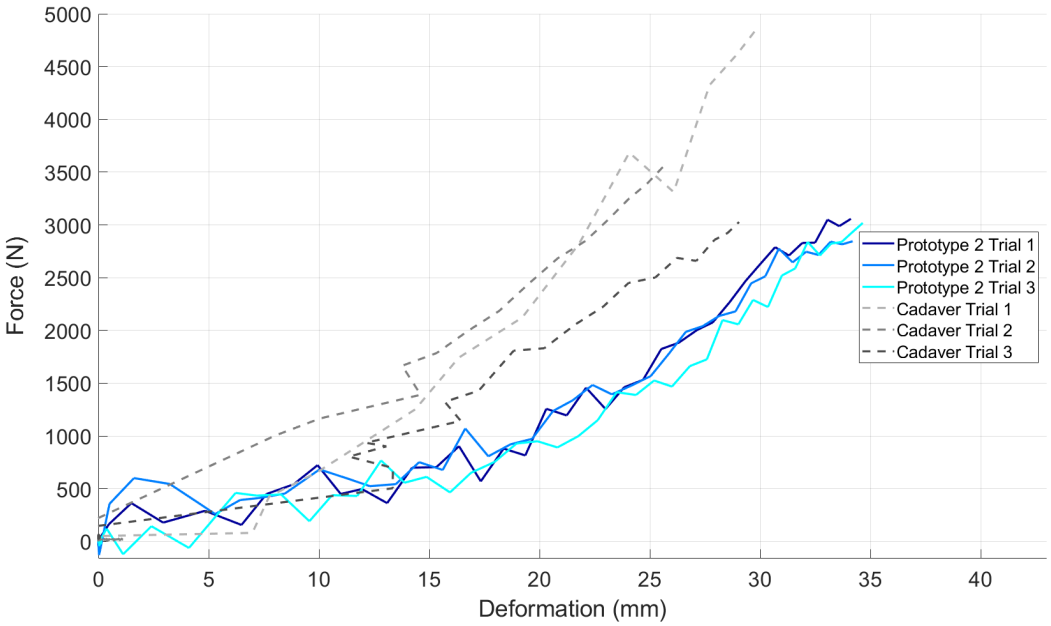


Figure 4.12: Force-deformation response of Prototype II vs Cadaver

Load Cell Response

To evaluate the performance of the embedded load cell, force measurements were recorded while the sensor was integrated with the foot form. Prototype II was impacted at 10 J for

ten trials and 15 J and 20 J energies for one trial outside the boot.

Figures 4.13 and 4.14 show the force versus energy response for accuracy and repeatability, respectively.

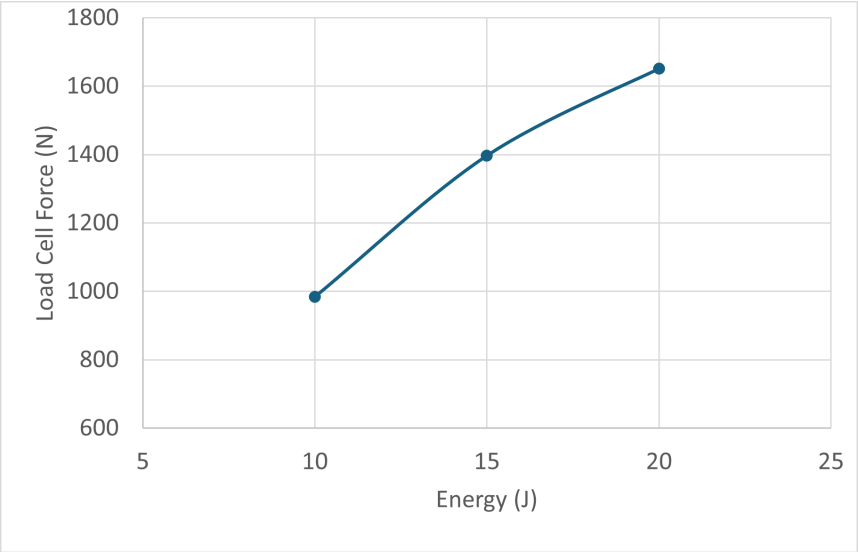


Figure 4.13: Load Cell Force vs Energy Response Accuracy - Prototype II

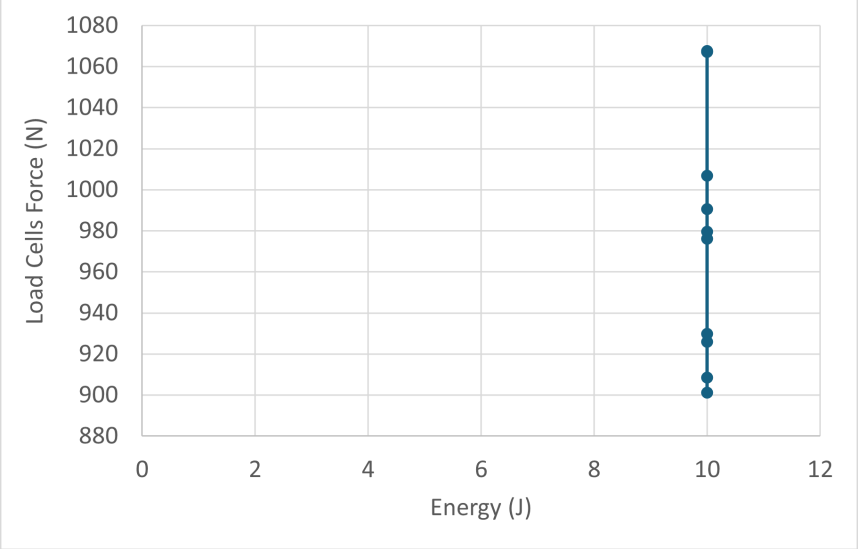


Figure 4.14: Load Cell Force vs Energy Response Repeatability - Prototype II

Benchmark

The foot form was subjected to three impact trials at 20J to establish benchmarks for metatarsal guard evaluation, and embedded load cell response was captured and tabulated in Table 4.6.

Table 4.6: Benchmark Testing for Prototype II

Trials	**Load (N)**			
	Load Cells		**Total**	**Impact**
	A	**B**	**A+B**	**Load Cell**
1	897.33	804.28	1701.61	2090.30
2	1005.91	821.82	1827.73	2165.84
3	826.91	776.82	1603.72	1987.53

In-Boot Validation with Engineered Foot Form

To evaluate the protective performance of metatarsal guards in safety footwear using the engineered foot form, three different boot models were tested. Each boot was subjected to 50 J and 100 J impact energy for three trials each. This test was designed to evaluate whether the impact force transmitted through each boot remained below the benchmark threshold established in the previous section, indicating sufficient or insufficient protection against metatarsal injury. Boot model configurations are listed in Table 4.7. During pilot testing, the embedded load cells saturated at 100 J, therefore, the results of all trials are summarized in Table 4.8. At 50 J, forces remained within the sensor range, and Figure 4.16 shows the mean of three trials for each of the three boot configurations for comparison.

Table 4.7: Specifications of safety footwear evaluated for metatarsal guard performance

Boot	Type	Specifications	Size
A	Hard Metatarsal Guard	Timberland PRO Endurance HD MG NT	US 9 Men
B	Soft Metatarsal Guard	Timberland PRO Endurance HD External Metguard	US 9 Men
C	No Metatarsal Guard	Timberland PRO Endurance HD NT WP	US 9 Men



Figure 4.15: Safety footwear evaluated for metatarsal guard performance

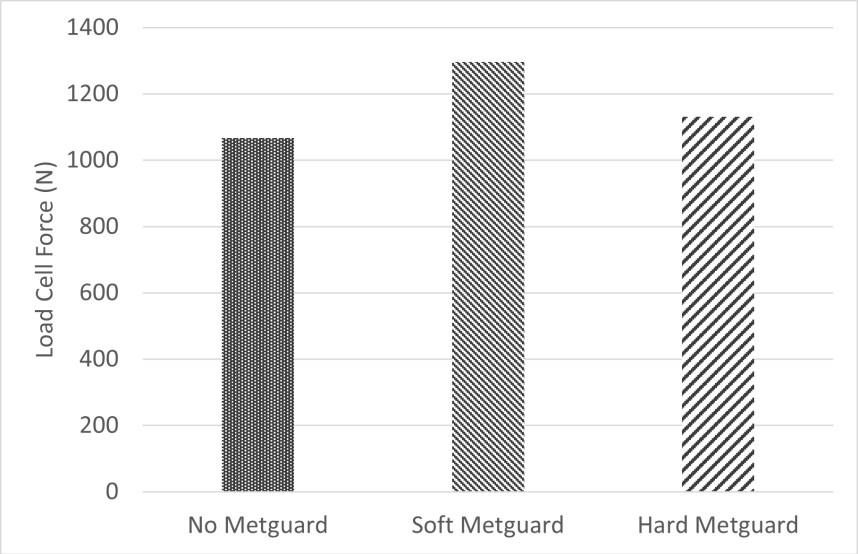


Figure 4.16: Transmitted mean force at 50 J for each boot using Prototype II

Table 4.8: Transmitted force at 100 J, for each boot using Prototype II

Type of Boot	**Trials**	**Load (N)**			
		Load Cells		**Total**	**Impact**
		A	**B**	**A+B**	**Load Cell**
No Metatarsal Guard	i	1063.88*	185.14	1249.02	4755.58
	ii	1063.88*	173.17	1237.06	4897.59
	iii	1063.88*	73.71	1137.59	5460.09
Soft Metatarsal Guard	i	1063.88*	220.18	1284.07	5059.69
	ii	1063.88*	186.66	1250.54	5284.69
	iii	1063.88*	145.03	1208.92	5476.95
Hard Metatarsal Guard	i	1063.88*	30.72	1094.60	6718.03
	ii	1063.88*	174.28	1238.16	5389.74
	iii	1063.88*	182.09	1245.97	5508.40

* Load Cells Oversatured

4.4.5 Limitations of Prototype II

Prototype II tackled the limitations of Prototype I. It demonstrated improved load-sensing capability with the two load cell system. After scaling, the foot form was easy to insert and remove from the boot. Moreover, the tibia components that were constrained at the bottom stayed constrained during impact testing. Despite addressing the concerns of the previous prototype, Prototype II presented its own set of limitations discussed subsequently.

1. Load Cell A, positioned at the front of the foot form, reached saturation when the foot form, positioned within the boot, was impacted at an energy level of 100 J. The load was transferred unevenly toward the front of the two–load cell system, despite the impact point being located approximately at the midpoint between the two load cells.

2. Prototype II did not accurately represent the geometry of the foot inside a boot. The medial arch of the foot and the dorsal slant of the foot model were more pronounced because initial foot model development did not account for load-bearing conditions.

These limitations prompted the development of Prototype III, discussed in the next section.

4.5 Prototype III

4.5.1 Conceptual Design

Experimental results from the previous prototypes revealed two major limitations: the load cell saturation at 100J inside the boot with load being transferred towards the front, and the issues with certain design artifacts of the initial foot model acquired from ASTM. To mitigate these problems, a third prototype was developed with a modified design to improve load distribution, overall performance, and geometry of the foot form.

The load distribution within the two load cell system is observed to be at the front of the foot despite impacting it at the centre. Therefore, to level the force shared between the two foot forms, the tunnel inside the foot form had to be moved ahead compared to Prototype II. To make this change, the midfoot section of the foot form was rescaled in a 2:1:1 ratio, in the x, y, and z axes, and merged with the forefoot and hindfoot sections. This modification increased the length of the foot form, and as the forefoot was moved

ahead, it accommodated the load cell enclosure, which earlier was not possible due to less material availability at the front.

Due to a length extension of the foot form, the original toe segment was removed and replaced with a shorter toe geometry to restore the overall length to that of the original 3D foot model of a US size 9 men's foot. The slant on the dorsal side of the foot model and the pronounced medial arch were addressed by reducing the material on top of the dorsal part of the foot form and adding material along the arch on the medial part of the foot form. Due to the reduction of material above the two-load-cell assembly, additional shielding was required to prevent the load cells from over-saturating. Accordingly, the lattice infill density of the foot form was increased from 55% to 75%.

To enhance modularity and manufacturing efficiency, the foot form was divided into two parts. These were assembled using an interference fit at the junction. The assembled foot form is shown in Figure 4.18, and components are listed in the Table 4.9.

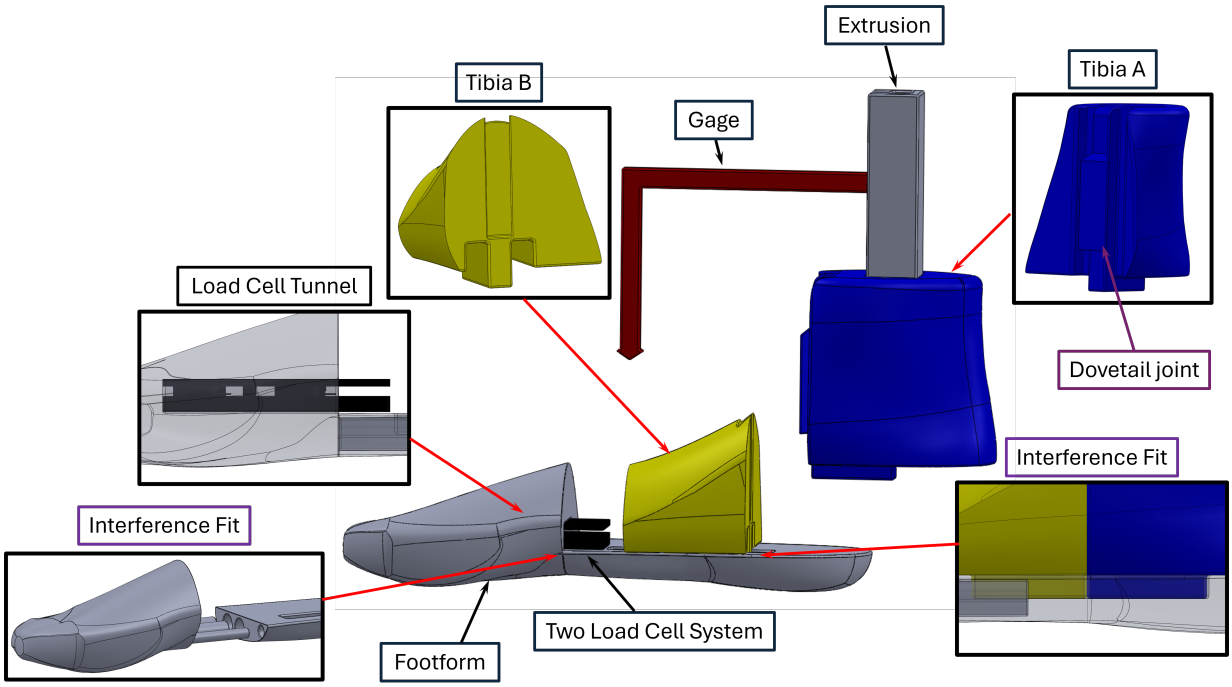


Figure 4.17: Concept Design of Prototype III

4.5.2 Manufacturability of Prototype III

Similar process parameters were followed for manufacturing Prototype III. The following table summarizes the manufacturing specifications and estimated print time of each component. Total manufacturing time if printed simultaneously is 12 hours. During assembly, the pins used to join the two foot form sections fractured, so the parts were bonded with a clear epoxy adhesive to restore structural integrity. The assembled Prototype III is shown in Figure 4.18

Table 4.9: Manufacturing Specifications - Prototype III

Component	**Technology Used**	**Material**	**Latticing Parameters**	**Time (hrs)**
Load Cells	Commercial Sensor	Stainless Steel	N/A	N/A
Foot Form	SLA (Formlabs 4)	Flexible 80A Resin	Cubic, 75%, 6.35 mm	12
Tibia A	FDM (Prusa i3 MK3)	PLA Filament	Gyroid, 10%	7
Tibia B	FDM (Prusa i3 MK3)	PLA Filament	Gyroid, 10%	3
Extrusion	FDM (Prusa i3 MK3)	PLA Filament	Gyroid,, 10%	3
Load Cell Enclosure	Custom Manufactured	Stainless Steel	Solid	N/A
Gage	FDM (Prusa i3 MK3) / FDM	PLA Filament	Gyroid, 10%	1



Figure 4.18: Prototype III

4.5.3 Experimental Testing

Prototype III underwent three test phases. Biofidelity was assessed by comparing its force–deformation response with cadaveric data at the target impact. The embedded load cells were impacted at five energies to obtain the total force response and identify saturation limits. A benchmark force threshold at 20 J was gathered, and in-boot performance was verified across three safety-boot configurations at four impact energies. Prototype III underwent three test phases. First, its force–deformation response was compared with cadaveric data at the target impact to assess biofidelity. Second, the embedded load cells were impacted at five energies to characterize the response and saturation limits. Third, a benchmark force threshold was derived at 20 J. Lastly, the foot form was evaluated in three safety-boot configurations at four impact energies to verify performance under in-boot conditions.

Biofidelity

The biofidelity of Prototype III was assessed by comparing the force-deformation response of Prototype III with cadaver feet at 33J impact energy. Figure 4.19 shows the response of the foot form compared to cadaver feet.

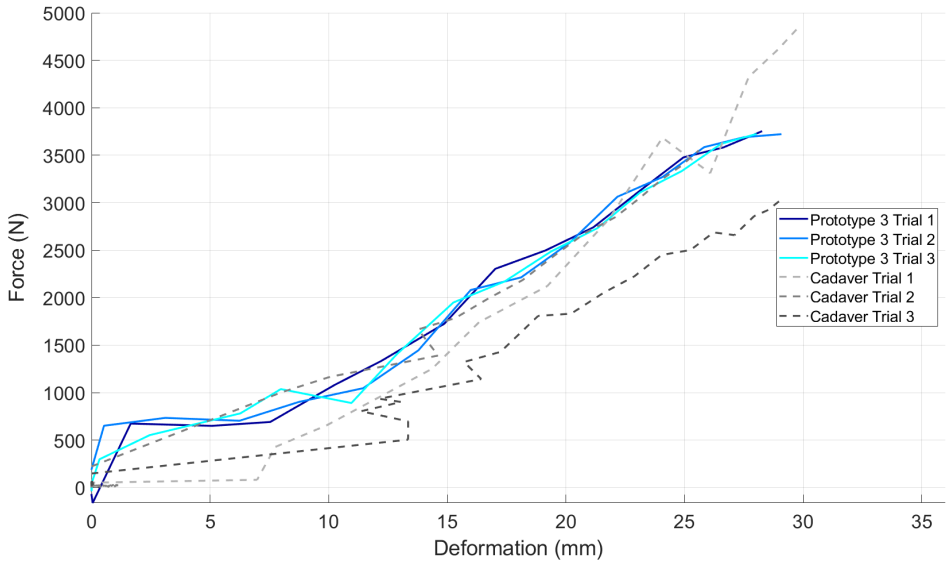


Figure 4.19: Force-deformation response of Prototype III vs Cadaver

Load Cell Response

Load cell response was evaluated at five different energies: 10J, 15J, 20J, 25J, and 30J, and tabulated below.

Table 4.10: Load Cell Response at various impact energies- Prototype III

Energy	**Trials**	**Load (N)**			
		Load Cells		**Total**	**Impact**
		A	**B**	**A+B**	**Load Cell**
10 J	i	608.22	774.16	1382.38	1542.08
	ii	634.84	712.10	1346.94	1473.35
	iii	684.16	738.30	1422.45	1578.06
	iv	927.97	551.78	1479.75	1566.07
	v	1034.31	524.74	1559.05	1602.70
15 J	i	1063.88*	531.26	1595.14	2358.09
	ii	1063.88*	550.68	1614.56	2452.44
	iii	1063.88*	482.79	1546.67	2513.06
	iv	1063.88*	441.48	1505.37	2347.07
	v	1063.88*	438.86	1502.74	2551.64
20 J	i	1004.39	1063.88*	2068.27	2421.31
	ii	1005.00	1063.88*	2068.89	2487.13
	iii	976.08	1063.88*	2039.97	2404.13
	iv	859.14	1063.88*	1923.02	2302.65
	v	961.30	1063.88*	2025.18	2493.93
25 J	i	1063.88*	635.75	1699.63	3334.92
	ii	1063.88*	671.15	1735.04	3271.70
	iii	1063.88*	653.48	1717.37	3411.10
	iv	1063.88*	666.36	1730.24	3347.56
	v	1063.88*	618.47	1682.35	3438.66
30 J	i	1063.88*	1063.88*	2127.77	3753.46
	ii	1063.88*	1063.88*	2127.77	3722.02
	iii	1063.88*	1063.88*	2127.77	3724.61
	iv	1063.88*	1063.88*	2127.77	3678.25
	v	1063.88*	1063.88*	2127.77	3628.00

* Load Cells Over-saturated

Benchmark

During pilot testing, it was observed that the load cell maxed out at 20J. The load cell response is tabulated in Table 4.11

Table 4.11: Benchmark Test at 20J - Prototype III

Trials	**Load (N)**			
	Load Cells		**Total**	**Impact**
	A	**B**	**A+B**	**Load Cell**
1	1004.39	1063.88*	2068.27	2421.31
2	1005.00	1063.88*	2068.89	2487.13
3	976.08	1063.88*	2039.97	2404.13
4	859.14	1063.88*	1923.02	2302.65
5	961.30	1063.88*	2025.18	2493.93

* Load Cells Over-saturated

In-Boot Validation with Engineered Foot Form

Each boot was impacted at 10, 20, 30, and 50 J for three trials each. At 10 and 20 J, load cell forces remained within range. Figures 4.20 and 4.21 present the mean transmitted force results for each boot configuration. At 30 and 50J, the embedded load cells saturated, so all trials at those energies are summarized in Tables 4.12 and 4.13.

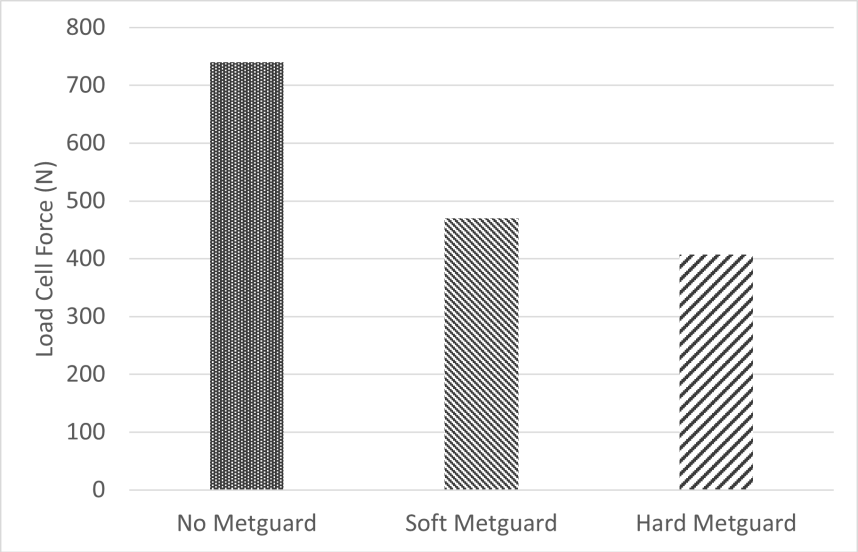


Figure 4.20: Transmitted mean force at 10 J for each boot using Prototype III

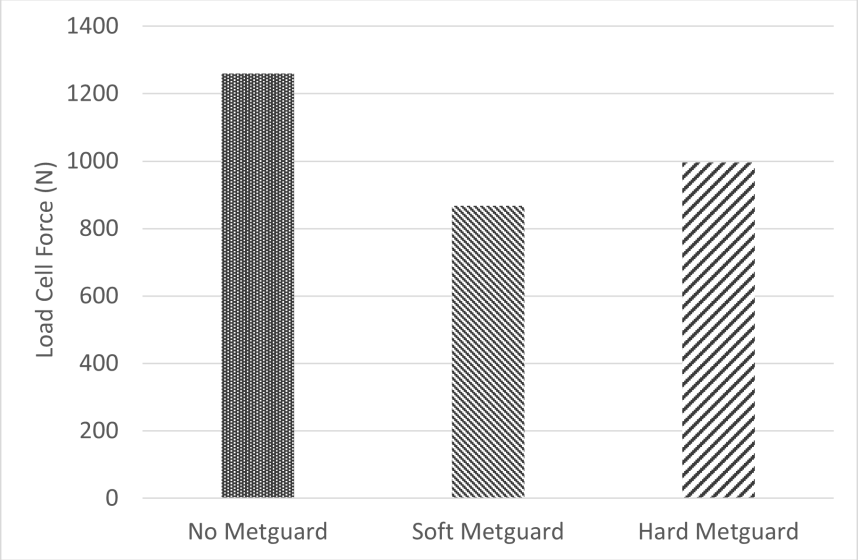


Figure 4.21: Transmitted mean force at 20 J for each boot using Prototype III

Table 4.12: Transmitted force at 30 J, for each boot using Prototype III

Type of Boot	**Trials**	**Load (N)**			
		Load Cells		**Total**	**Impact**
		A	**B**	**A+B**	**Load Cell**
No Metatarsal Guard	i	1063.88*	431.08	1494.96	2124.67
	ii	1063.88*	364.45	1428.34	2229.06
	iii	1063.88*	216.81	1280.69	2642.42
Soft Metatarsal Guard	i	996.38	433.80	1430.18	2190.48
	ii	1063.88*	301.43	1365.31	2257.27
	iii	1063.88*	380.96	1444.84	2314.00
Hard Metatarsal Guard	i	954.62	411.37	1365.98	2170.70
	ii	924.98	394.54	1319.52	2116.56
	iii	1029.87	416.62	1446.49	2283.85

* Load Cells Over-saturated

Table 4.13: Transmitted force at 50 J, for each boot using Prototype III

Type of Boot	**Trials**	**Load (N)**			
		Load Cells		**Total**	**Impact**
		A	**B**	**A+B**	**Load Cell**
No Metatarsal Guard	i	1063.88*	874.11	1938.00	3448.39
	ii	1063.88*	1010.77	2074.66	3710.99
	iii	1063.88*	1046.15	2110.03	3951.88
Soft Metatarsal Guard	i	1063.88*	871.13	1935.01	3284.34
	ii	1063.88*	115.82	1179.71	3911.68
	iii	1063.88*	141.76	1205.64	4005.05
Hard Metatarsal Guard	i	1063.88*	474.07	1537.95	4019.64
	ii	1063.88*	557.81	1621.69	3983.97
	iii	1063.88*	789.53	1853.41	3812.79

* Load Cells Over-saturated

4.6 Chapter Summary

This chapter detailed the design, fabrication, and validation of an instrumented, biofidelic foot form for metatarsal impact testing, guided by a structured engineering design framework. Requirements emphasized cadaveric biofidelity, accurate and repeatable force measurement at the metatarsals, durability under repeated loading, and modularity for repair and iteration.

Prototype I established feasibility using a Flexible 80A foot form with a single miniature load cell. Although its force–deformation response fell within the cadaveric corridor at 33 J, the small sensing footprint produced variable readings, fit within the boots was challenging, and the tibia interface migrated under load. Prototype II addressed these issues with a two–load-cell architecture validated on a $2 \times 3 \times 2$ in resin cuboid at 10 J, a weight-bearing geometry scale adjustment, and improved tibia constraints. In-boot tests at 50 J remained within range, but at 100 J, the front cell saturated consistently.

Prototype III refined geometries, such as midfoot rescaling, dorsal and arch corrections, moved and shielded the sensing tunnel, and increased lattice density to 75% to improve load sharing. It reproduced the force-deformation response of the cadaver at 33 J, captured the load cell response and and completed in-boot tests at 10, 20, 30, and 50 J. However, saturation occurred at higher energies.

The next chapter discusses these results, examines sources of variability and boundary-condition sensitivity, and outlines recommendations for future work to develop better standards.

Chapter 5

Discussion

This research presents an improvement to the current ASTM standard, which tests the performance of safety shoes for metatarsal protection, by designing and developing a biofidelic instrumented foot form. This is achieved by understanding the limitations of the current standard and developing a foot surrogate that has similar mechanical properties to a cadaver foot and has a reliable measurement method. The biofidelic foot form surrogate developed measures the force transmitted to the metatarsals under impact loading. This chapter provides a detailed analysis of the results obtained in Chapters 3 and 4. Section 5.1 discusses the use of additive manufacturing to optimize material properties. Sections 5.2 and 5.3 discuss the iterative design and performance of the developed prototypes of instrumented foot forms.

5.1 Computational and Experimental Approaches in Material Selection

In Chapter 3, a combination of computational and experimental methodology was used to obtain the force-deformation response of various materials. DfAM principles helped create an engineered material that approximates the mechanical behaviour of the human foot during impact. Pre-screening using simulation models was used to reduce the initial prototyping costs associated with experimental testing and helped obtain vital information regarding material behaviour, which was applied later to experimental methodology.

In Section 3.3.1, a FE Model was developed in which the foot form's material properties were varied, and the resulting force-defomation responses of five materials were compared,

and the force-defomation response of the viable material, 8% sulphur vulcanized rubber, was plotted in Figure 3.4. The 8% sulphur vulcanized rubber exhibits a force-deformation response that aligns closely with cadaveric data. The area under the force-deformation curve shows part of energy read by the loadcell, and not the total energy applied. Moreover, it is observed that the rate of loading differs slightly. This divergence could be attributed to the initial conditions used in the finite element analysis.

The model was developed as a tool to aid material selection rather than as a definitive simulation of foot mechanics. The model did not undergo preloading due to gravity and bodyweight to simulate arch flattening as suggested by Miller through his arch models [10]. This could be the contributing factor to the more pronounced deformation behaviour observed. Future models aiming to simulate biological foot behaviour should incorporate pre-loading conditions and consider hexahedral meshing as opposed to the tetrahedral meshing currently used to enhance the fidelity of the model. This aligns with a study by Song et al. (2022) [87] that specifies boundary conditions for modelling a foot under loading and recommends applying bodyweight load at the tibia (proximal end) while developing an FEA model. Although 8% sulphur vulcanized rubber emerged as a strong candidate, conventional manufacturing costs outweighed the benefits. Therefore, a shift to additive manufacturing was chosen. Additive manufacturing supports rapid prototyping and iterative design, and the initial costs of prototyping are low, as stated by Bikas et al. (2016) [34].

After evaluating foot sections across different lattice patterns and infill densities, a full foot form made completely of Ninjaflex TPU with 70% infill cubic lattice was found as a potential material for the surrogate. The response obtained was similar to the force-deformation response behaviour of the human foot. In Figure 3.7, initially, the curve deforms with a high rate of deformation but lower forces. This can be attributed to the collapse of the arch as the testing is performed on a foot form with a complete planar surface and homogeneous material makeup of the manufactured foot form. The foot form manufactured lacks any embedded load sensors. In literature, surrogate development includes a rigid body inside that mimics the bone. Alessa et al. (2023) made a surrogate hand composed that inculcated 3D printed bones and Hrysomalis, which developed a thigh surrogate, used a stainless steel rod to mimic the femur bone [30, 33]. Introducing an internal rigid body using in-situ force sensors is therefore expected to further align with the force-deformation behaviour of the foot. Moreover, out of the lattices tested, the cubic lattice performs the best for this application. Cubic lattices in literature demonstrate similar behaviour. Ozemediz discussed that the cubic lattice, compared to other lattices at the same infill density, under compressive loading distributed the loads most effectively and reduced the impact stress overall. [56].

Due to limitations with regard to longer print times that spanned days, SLA technology was utilized for its faster print time and availability of Flexible 80A as a resin, which mimics the behaviour of TPU. A comparison study between the two materials was devised to find an engineered configuration of Flexible 80A that closely aligns with that of Ninjaflex TPU. Cuboids with identical external dimensions but different internal lattice structures were manufactured and tested with an experimental drop tower setup at 33J impact energy. Holding geometry constant enables direct comparison of lattice-driven force–deformation behaviour while reducing material use and prototyping time. Therefore, instead of printing full foot forms for a comparison study, cuboids were utilised.

Figure 3.9 shows almost identical force transmitted and deformation patterns between latticed Flexible 80A resin and latticed Ninjaflex TPU. Therefore, 55% cubic infill Flexible 80A resin can be an ideal alternative to 70% cubic infill Ninjalfex TPU. Therefore, a foot form manufactured with Flexible resin having a cubic lattice pattern, 55% infill density, *6.35 X 6.35 X 6.35 mm* unit cell size, and a load sensor embedded inside made of stainless steel or a rigid material would exhibit a similar response to that of a cadaver. This hypothesis proves to be true and is observed in Prototype I's cadaver response (Figure 4.5).

5.2 Iterative Design of Instrumented Foot Form

Instrumented prototypes of foot forms were designed and developed in Chapter 4 through an iterative process that followed the design framework by Pahl and Beitz [85]. After the initial design was based on design requirements, subsequent prototype designs were built using the design requirements and limitations of the previous iteration. This iterative methodology is followed in the study by Klein [28] and Hrysomallis [30], where an ankle is developed for biomechanical testing of footwear and a thigh surrogate is developed for testing the impact resistance of cricket pads. The three prototypes built for this study are shown in Figure 5.1.

The force-deformation response obtained from the three prototypes differed but fell within the corridors of cadaveric data, suggesting that the engineered foot forms demonstrate comparable mechanical behaviour to the human foot. Biofidelity is essential because a surrogate that does not mirror human response cannot yield accurate estimates of protection provided by metatarsal guards. Apart from the material properties of additively manufactured latticed structures, three key factors influence the cadaveric force-deformation responses:



Figure 5.1: Three Prototypes: A- Prototype I, B- Prototype II, C- Prototype III

Longitudnal Arch Collapse

Miller et al. (1987) [10] talk about the two models of longitudinal arch and explain that during weight-bearing activities, the longitudinal arch of the foot flattens slightly. When the initial model of the foot was developed by ASTM, the foot was not load-bearing. Therefore, the arch observed in the foot is more pronounced. This effect impacts the current designs. Therefore, the arch height in Prototype III was deliberately reduced to align with conditions of the foot under loading inside footwear, as seen in human feet. This is illustrated in Figure 5.2.

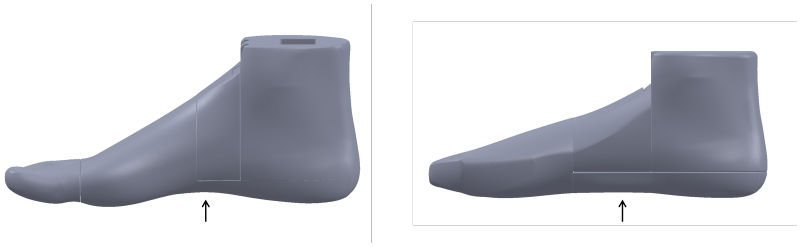


Figure 5.2: Arches differences between Prototypes II and III

Material Width at Load Cell Junction

During the transition from Prototype I to Prototype II, the load cell tunnel was repositioned forward to align better with impact zones inside the boot and to improve the load sharing between the two load cells. While this shift allowed for better measurement, it also introduced a thinner cross-section at the junction as shown in Figure 5.3. The reduction in material width increased flexibility at the junction, making the design more prone to deformation under impact loads. This design artifact in Prototype III, when epoxy was used to join the parts together, reduced the flexibility.

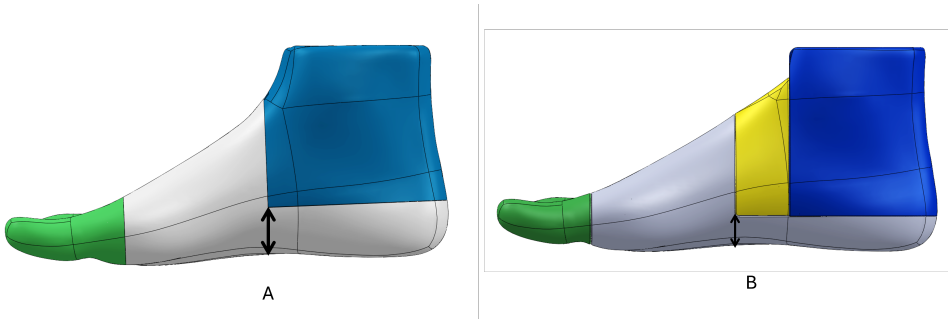


Figure 5.3: Difference between material width in Prototype I (B) and Prototype II (A)

Composite Structure of Surrogate

All three prototypes function as composite structures composed of a soft, flexible outer layer made of latticed Flexible 80A resin and internal components that include stainless steel plates with load cells or a single load cell. This layered design allows the foot forms to replicate the heterogeneous nature of human body parts. The addition of a stainless steel load cell enclosure was intended to provide better force transmission under repeated testing. A similar approach was used in a study by Alessa et al. (2023) [33] where 3D printed bones were embedded in a hand surrogate to test the protective performance offered by impact resistance gloves. Another study by Hrysomalis [30] used a stainless steel rod to replicate a femur in a thigh surrogate. The work supports the notion that biomechanical surrogates may integrate multiple materials with distinct stiffness to mirror real anatomical response.

All prototypes combined rigid PLA components with flexible latticed components. Using PLA for the rigid elements reduced cost, shortened print times, and helped manage build-volume constraints. The toe segments in Prototype I and Prototype II were printed in PLA and integrated with the flexible lattices due to constraints of the printer. The

resin printer, Formlabs 4, has a limited build volume, so Prototype III was produced in two sections and joined with epoxy after the pins failed. Future work should evaluate more robust joining strategies, such as dovetail joints, to replace epoxy, or eliminate the joint by printing the full foot form in a single build on a Formlabs 4L, whose build capacity is approximately five times that of the current Formlabs 4.

5.3 Performance of Instrument Foot Forms

In Chapter 4, the design and performance testing of three prototype foot surrogates are discussed. The design decisions were discussed in the previous section. This section will discuss the performance of the instrumented foot forms based on the evaluation of two facets: Load cell performance and In-boot testing performance.

Load Cell Performance

Load-cell responses for Prototypes II and III were recorded across multiple impact energies to understand the relationship between applied energy and transmitted force. For Prototype II, forces increased linearly from 10 to 20 J, indicating that as impact energy increases, the forces read by the load cells increase as well. At 10 J, the total measured force by the two load cells in Prototype II ranged from 901.2 N to 1067.5 N (mean 975.372 and SD ±60.23). For Prototype III at the same energy, total load cell force ranged from 1382.38 N to 1559.05 N (mean 1438.12 and SD ±83.70). Both prototypes individually observed some variation in forces, but it is substantially lower than in the single load cell force measurement system.

Prototype I, which utilizes one load cell system, underwent initial benchmark tests at 20 J impact energy. The benchmark thresholds were set up in consultation with ASTM. A 10% injury-risk probability was selected as the criterion for evaluating metatarsal guard performance. On the injury-risk curve, a 10% fracture probability corresponds to a 20 J impact energy applied directly to the foot form. The force recorded by the embedded sensors under this condition was established as the benchmark. For all safety boot tests at higher energies, the transmitted force was required to remain below this threshold. Benchmark testing at 20J conducted directly on Prototype I (Table 4.3) showed large variability in the embedded load-cell readings, a standard deviation of $\pm 153.77N$, with one trial recording the lowest value at 270.81 N, while the highest was recorded at 578.78 N. This large difference indicates that a single load cell force sensing system is not reliable

for capturing the total transmitted load when compared to the two load sensing systems. A likely contributor is the small effective sensing area in Prototype I (Figure 4.7).

Two load cell validation results further support this configuration 4.4. When impacts were applied at three locations on a flat, even top surface, the difference between the highest and lowest total force recorded by two load cells was 6.4%. As the impact location shifted from Point I to Point III, the force recorded by load cell A decreased while load cell B increased, with the sum remaining effectively consistent with stable load sharing. These tests were performed at an energy of 10J. At higher energies, 30J, capacity limits of the load cells were encountered for Prototype II and Prototype III. This is a current limitation of the study. Higher-capacity sensors (e.g., miniature load-washer cells of 1 in diameter) are recommended for further validation [88].

The robustness of the two-load cell system is important in metatarsal performance evaluation tests, where exact targeting over a single sensor is difficult even with the use of a gauge. A dual-sensor system provides a wider effective sensing area and maintains consistent total force even when the impact is off-centre. The difference between the loading sensing area between Prototype I and Prototype III is shown in Figure 5.4.

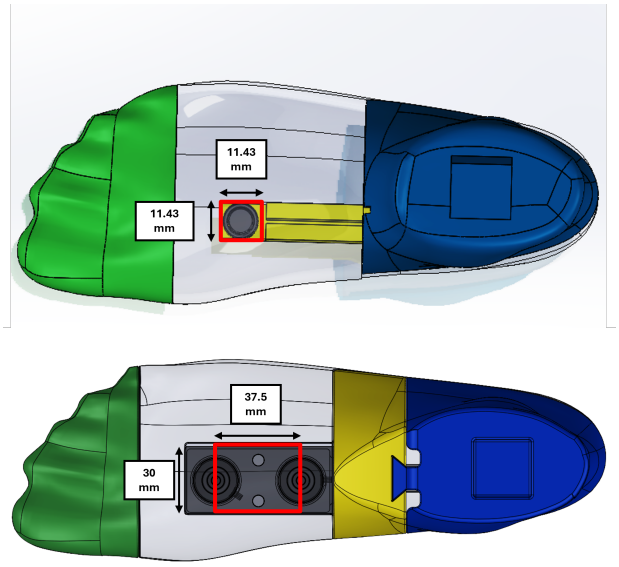


Figure 5.4: Load sensing area difference between single vs dual load cell system

In-Boot Testing Performance

The impact performance testing of metatarsal guards in boots was performed with Prototypes II and III at various energies. Prototype II was tested at 50J and 100J. The initial pilot testing was performed in correlation with ASTM standards at 100J. However, this oversaturated the load cells. Therefore, lower energies were chosen as well.

For Prototype II, Figure 4.16, at 50J impact energy the results show that the boot without a metatarsal guard recorded force of $1066.295 \pm 27.81N$ (mean $\pm$ standard deviation), which is lower than the forces measured for the soft metatarsal guard ($1295.6 \pm 50.11N$) and hard metatarsal guard ($1131 \pm 66.05N$) at an impact energy of 50 J. This outcome is counterintuitive, as metatarsal guards are generally intended to reduce transmitted force; in this case, the opposite trend was observed. One possible explanation lies in the interaction between the foot form and the boot. In Prototype II, the dorsal surface of the foot form was arched higher than typical human foot anatomy. Moreover, as noted by Feeney [32], safety footwear manufactured using traditional "U-throat" construction methods for protective footwear often results in a complex and uneven fit when worn. The hypothesis is that this mismatch produced an uneven force transmission within the boot–foot form system, leading to skewed results. Furthermore, Demichelis [31] reported similar fit issues in her foot surrogate used for thermal insulation testing, noting that surrogates do not compress within the boot in the same way as a human foot.

For Prototype III, the impact testing was performed at 10J, 20J, 30J, and 50J when initial pilot testing revealed that load cells reached maximum capacity at 100J. At 30J and 50J energies, the load cells were oversaturated. For energies 10J and 20J, Figure 4.20 and Figure 4.21, the no-metatarsal guard boot recorded the highest transmitted forces by the two embedded load cells across all categories, measuring $739.87 \pm 15.01N$ at 10 J and $1259.35 \pm 102.58N$ at 20 J. The soft metatarsal guard provided the greatest level of impact protection at 20 J, with a transmitted force of $867.06 \pm 65.28N$, compared to $469.60 \pm 7.56N$ at 10 J. In contrast, the hard metatarsal guard offered the best protection at 10 J, $407.16 \pm 25.71N$, but a higher transmitted force of $995.85 \pm 42.03N$ at 20 J. These results suggest that the protective performance of soft and hard metatarsal guards is better than boots without metatarsal guard protection. Current literature offers no conclusive evidence regarding whether soft or hard metatarsal guards provide superior impact protection, indicating the need for further comparative studies. Out of all three iterations of foot surrogates developed, Prototype III demonstrated improved capability for evaluating metatarsal impact resistance in protective footwear. This improvement is attributed to the reduced dorsal surface angle, which allowed for a better fit between the foot form and the upper portion of the boot, thereby promoting more uniform force

distribution across the embedded load cells.

At higher energies, specifically 100 J for Prototype II (Table 4.8) and 30 J and 50 J for Prototype III (Tables 4.12 and 4.13), Load Cell A consistently reached its maximum capacity. The point of impact on the boot coincided with the centreline between the two load cells; however, a consistent trend was observed in which Load Cell A (front) registered higher forces than Load Cell B (rear). This can be due to uneven interaction between the boot and the foot form inside the boot. This discrepancy may be attributed to uneven interaction between the boot and the foot form within the boot. The issue could be mitigated by employing higher-capacity load cells to ensure that the total transmitted force is accurately captured, even when the majority of the load is borne by Load Cell A.

Eliminating oversaturation of force sensors would allow accurate computation of benchmark thresholds for Prototype III and allow for a systematic evaluation of both integrated and external metatarsal guards. In addition, current standards specify an impact location 89mm from the toe toward the heel, which does not coincide with the mid-metatarsal region and more closely aligns with the midpoint of many metatarsal guards. This discrepancy requires further evaluation and may justify refining the impact-location specification. Among the prototypes, Prototype III combines biofidelity and geometry with an appropriate force-measurement system. Moreover, upon visual inspection, no evidence of damage is observed. This can be further validated by the consistent results demonstrated by the foot form across more than 150 trials with varied impact energies. Therefore, Prototype III is a viable candidate for further development toward replacing the wax surrogate in ASTM standards (F2412).

5.4 Summary

This is the first study to design, instrument, and validate a foot surrogate specifically for evaluating metatarsal guards in safety footwear under ASTM standards. This contribution provides a practical pathway to more repeatable, force-based evaluation of metatarsal protection. Across prototypes, the dual-sensor configuration marked lower variability than a single sensor. The effect of metatarsal guards was observed in Prototype III, suggesting the protection offered by them when compared to no metatarsal guards in protective footwear. Accordingly, Prototype III had the best consistent measurements for evaluation and should be further developed as the reference surrogate. These findings support a force-based measurement system for metatarsal protection testing and demonstrate the feasibility of an instrumented surrogate for standards development.

Chapter 6

Thesis Conclusions

6.1 Summary

The primary objective of this study was to develop and validate an instrumented, biofidelic foot form for evaluating the metatarsal impact resistance of protective footwear per ASTM testing methodologies. Existing test surrogates, such as wax foot forms, had its shortcomings that limited their ability to predict fracture risk. To address this gap, a combination of computational modelling, experimental testing, and additive manufacturing techniques was employed to iteratively design, fabricate, and evaluate the developed prototype foot form for biofidelity and efficacy in evaluating the protective footwear for metatarsal protection.

The material selection process identified Flexible 80A resin, when configured with optimized lattice parameters, as capable of producing a mechanical response closely aligned with cadaveric force–deformation behaviour. Additive manufacturing was adopted to enable rapid prototyping, modular design, and cost-effective iteration. Each prototype was evaluated through a series of drop tests, both directly on the foot forms and inside protective boots, using embedded force measurement systems and an external force and displacement acquisition setup.

The results demonstrated that all three prototypes produced force–deformation curves within cadaveric corridors, with Prototypes I and III showing the closest alignment. Design refinements addressing load cell placement, dorsal surface geometry, and composite structure significantly improved measurement reliability and fit inside footwear. Prototype III, in particular, offered enhanced load-sharing between sensors and reduced variability

during in-boot testing. However, at high energies, the load sensors reached their limit, and drop testing results according to ASTM standards could not be gathered. Neither soft nor hard metatarsal guards consistently outperformed the other, highlighting the need for further investigation into energy-dependent protection mechanisms. Fit and geometry mismatches between the surrogate and boot, common in traditionally manufactured safety footwear, were identified as factors influencing measurement variability.

The developed novel instrumented foot form, Prototype III, demonstrates strong potential as a repeatable and anatomically accurate surrogate for metatarsal impact testing. By providing direct force measurements at metatarsals, it enables a more accurate assessment of injury risk compared to deformation-only metrics. This work supports the argument for revising current ASTM standards to incorporate force-based criteria, aligning with approaches seen in other PPE testing standards.

6.2 Limitations and Future Work

While the developed instrumented foot forms show promising performance as surrogates for metatarsal impact testing, the following areas warrant further investigation and refinement:

1. Current foot form was derived without weight-bearing conditions. Therefore, the geometry of the foot form should be refined using weight-bearing 3D scans to more accurately capture the deformation of the medial arch and other anatomical features under load.

2. The miniature load cells saturated at higher impact energies, warranting the use of high-capacity load cells. For further development, high-capacity load cells with compact form factors should be implemented to prevent signal saturation at higher impact energies and to improve measurement reliability.

3. The data acquisition system used currently can be easily replaced by a low-cost, standalone data acquisition system and, therefore, can be developed and integrated, enabling the surrogate to be used effectively in industrial and field testing environments.

4. FE Model currently used does not emulate appropriate boundary conditions. A detailed computational model of the foot surrogate can be developed to simulate different boot constructions and metatarsal guard types, thereby reducing the cost and time associated with physical prototyping.

5. Instead of a force-based measurement system, a pressure-sensing measurement methodology can be applied to sense pressure upon impact.

6. Measurement systems could be replaced with engineered biofidelic dovels pin that replicates the behaviour of metatarsal bones. These pins can fit inside the tunnel situated along the metatarsal region and, upon impact, be inspected to see if they break.

References

[1] National Safety Council. Work injuries and illnesses by part of body, 2021-2022.

[2] Aaron S. Banks, Michael S. Downey, David E. Martin, and Stephen J. Miller. Metatarsal fractures. In Aaron S. Banks, Michael S. Downey, David E. Martin, and Stephen J. Miller, editors, *McGlamery's Comprehensive Textbook of Foot and Ankle Surgery*, pages 1775–1790. Lippincott Williams & Wilkins, Philadelphia, PA, 2001.

[3] Paul Tornetta, William M. Ricci, Margaret M. McQueen, and Charles M. Court-Brown. Fractures and dislocations of the midfoot and forefoot. In *Rockwood and Green's Fractures in Adults*, pages 2689–2697. Lippincott Williams & Wilkins, Philadelphia, PA, 8 edition, 2015.

[4] J. R. Clements and R. Schopf. Advances in forefoot trauma. *Clinics in Podiatric Medicine and Surgery*, 30(3):435–444, 2013.

[5] ASTM International. Astm f2412-24: Standard test methods for foot protection, 2024.

[6] *CSA Z195:14 (R2023) – Protective Footwear*. CSA Group, Toronto, Ontario, 7 edition, 2014. Reaffirmed in 2023.

[7] Xavier Roothaer. *Multi-scale Study of the Mechanical Behaviour of Bearing and Bone-Bearing Bones: Towards Personalization of FE Human Models*. Phd thesis, Université Polytechnique Hauts-de-France, France, 2019. NNT: 2019UPHF0020.

[8] Keith L. Moore, Arthur F. Dalley, and Anne M. R. Agur. *Clinically Oriented Anatomy*. Lippincott Williams & Wilkins, Philadelphia, 7 edition, 2013.

[9] Blausen.com staff. Medical gallery of blausen medical 2014. *WikiJournal of Medicine*, 1(2), 2014.

[10] J. E. Miller, M. B. Pohl, and W. Liu. Characterization of the foot as a shock absorber during the heel strike phase of gait. *Foot & Ankle International*, 8(1):3–14, 1987.

[11] Margareta Nordin and Victor H. Frankel. *Basic Biomechanics of the Musculoskeletal System*. Lippincott Williams & Wilkins, Philadelphia, PA, 4 edition, 2012.

[12] Valentina Danesi, Luca Cristofolini, Mateusz M. Juszczyk, Paolo Erani, and Marco Viceconti. Mechanical properties of the human metatarsal bones. *Journal of Mechanics in Medicine and Biology*, 12(4):1250062, 2012.

[13] David J. Gutekunst, Tarpit K. Patel, Kirk E. Smith, Paul K. Commean, Matthew J. Silva, and David R. Sinacore. Predicting ex vivo failure loads in human metatarsals using bone strength indices derived from volumetric quantitative computed tomography. *Journal of Biomechanics*, 46(4):745–750, 2013.

[14] Mayank Kalra, Robert Bahensky, Stewart D. McLachlin, Duane S. Cronin, and Naveen Chandrashekar. In-situ fracture tolerance of the metatarsals during quasi-static compressive loading of the human foot. *Journal of Biomechanical Engineering*, 144(041001), November 2021.

[15] Anita Fung, Lindsay L. Loundagin, and W. Brent Edwards. Experimental validation of finite element predicted bone strain in the human metatarsal. *Journal of Biomechanics*, 60:22–29, 2017.

[16] T. Fujikawa, Y. Asano, T. Nishimoto, and R. Nishikata. Static fracture tolerance of human metatarsal in being run over by robot. In *2017 IEEE/RSJ International Conference on Intelligent Robots and Systems (IROS)*, pages 6935–6942, 2017.

[17] Mayank Kalra, Martine E. McGregor, Stewart D. McLachlin, Duane S. Cronin, and Naveen Chandrashekar. Characterizing in-situ metatarsal fracture risk during simulated workplace impact loading. *Journal of Biomechanical Engineering*, 145(5):051008, 2023.

[18] Denise M. Oleske, Jerome J. Hahn, and Maria Leibold. Work-related injuries to the foot: Data from an occupational injury/illness surveillance system. *Journal of Occupational Medicine*, 34(6):650–655, 1992.

[19] Anand Vora and Mark S Myerson. Crush injuries of the foot in the industrial setting. *Foot and Ankle Clinics*, 7(2):367–383, 2002.

[20] Naohiro Shibuya, Matthew L. Davis, and Daniel C. Jupiter. Epidemiology of foot and ankle fractures in the united states: An analysis of the national trauma data bank (2007 to 2011). *The Journal of Foot and Ankle Surgery*, 53(5):606–608, 2014.

[21] Lydia M. Kocher, Jonisha P. Pollard, Ashley E. Whitson, and Mahiyar F. Nasarwanji. Effects of metatarsal work boots on gait during level and inclined walking. *Journal of applied biomechanics*, 36(5):284–291, October 2020.

[22] Overlook Boots. What are metatarsal boots and how they work. https://www.overlookboots.com/blogs/boots/what-are-metatarsal-boots-and-why-get-them. Blog article; accessed 2025-08-13.

[23] Alison Nestel-Patt. Evolution of the met guard. *Occupational Health & Safety* (OH&S Online), January 2015. Accessed 2025-08-13.

[24] Ed Stone. Beyond the toe: The perks of metatarsal boot covers. https://bootworld.com/blogs/advantage/beyond-the-toe-the-perks-of-metatarsal-boot-covers, August 2024. Boot World blog; accessed 2025-08-13.

[25] Infrastructure Health & Safety Association. *Construction Health and Safety Manual*, chapter 10. Infrastructure Health & Safety Association, Etobicoke, Ontario, reprint edition, 2019. Chapter 10, Reprinted August 2019.

[26] Alberto Arceri, Antonio Mazzotti, Sofia Gaia Liosi, Simone Ottavio Zielli, Elena Artioli, Davide Golinelli, Lorenzo Brognara, and Cesare Faldini. What's the impact of safety footwear on workers concerning foot-related problems? a systematic review. *Healthcare*, 12(15), 2024.

[27] Thomas Payne, Sean Mitchell, and Richard Bibb. Design of human surrogates for the study of biomechanical injury: A review. *Critical Reviewstrade; in Biomedical Engineering*, 41(1), 2013.

[28] Michael J. Klein. *Development and Validation of a Surrogate Ankle for Biomechanical Testing of Footwear*. M.s., Michigan State University, United States – Michigan, 2018.

[29] Subhodip Chatterjee, Shubham Gupta, and Arnab Chanda. *Development of a Biomechanical Human Heel Surrogate for Barefoot Slip Testing*, page 257–271. Springer Nature, Singapore, 2024.

[30] Con Hrysomallis. Surrogate thigh model for assessing impact force attenuation of protective pads. *Journal of Science and Medicine in Sport*, 12(1):35–41, January 2009.

[31] Simone Demichelis. *3D-Printed Foot Manikin For Determining Thermal Insulation Of Footwear*. laurea, Politecnico di Torino, October 2023.

[32] Dan Feeney. Forging a confident connection to footwear. Magazine article.

[33] Faisal M. Alessa and Eduardo M. Sosa. Experimental evaluation of impact-resistant gloves using surrogate hands. *International Journal of Occupational Safety and Ergonomics*, 29(1):431–443, January 2023.

[34] Harilaos Bikas, Panagiotis Stavropoulos, and George Chryssolouris. Additive manufacturing methods and modelling approaches: A critical review. *The International Journal of Advanced Manufacturing Technology*, 83:389–405, 2016.

[35] Olaf Diegel, Axel Nordin, and Damien Motte. *Introduction to Additive Manufacturing*, chapter 1. Springer Series in Advanced Manufacturing. Springer, Singapore, 2019.

[36] Tuan D. Ngo, Alireza Kashani, Gabriele Imbalzano, Kate T. Q. Nguyen, and David Hui. Additive manufacturing (3d printing): A review of materials, methods, applications and challenges. *Composites Part B: Engineering*, 143:172–196, June 2018.

[37] Preethi Lakkala, Siva Ram Munnangi, Suresh Bandari, and Michael Repka. Additive manufacturing technologies with emphasis on stereolithography 3d printing in pharmaceutical and medical applications: A review. *International Journal of Pharmaceutics: X*, 5:100159, 2023.

[38] Ruben Kristiawan, Fitrian Imaduddin, Dody Ariawan, Ubaidillah Sabino, and Zainal Arifin. A review on the fused deposition modeling (fdm) 3d printing: Filament processing, materials, and printing parameters. *Open Engineering*, 11:639–649, 04 2021.

[39] Netrapal Singh, Hafsa Siddiqui, Bhavani Koyalada, Ajay Mandal, Viplov Chauhan, Sathish Natarajan, Satendra Kumar, and Manoj Goswami. Recent advancements in additive manufacturing (am) techniques: A forward-looking review. *Metals and Materials International*, 29:1–18, 01 2023.

[40] ASTM International and ISO. Iso/astm 52910:2018 – additive manufacturing—design: Requirements, guidelines and recommendations, 2018. Standard Specification.

[41] H. Bikas, A. K. Lianos, and P. Stavropoulos. A design framework for additive manufacturing. *The International Journal of Advanced Manufacturing Technology*, 103(9):3769–3783, August 2019.

[42] Formlabs. Form 4 design guide. White paper.

[43] Proto3000. Fdm 3d printing design guidelines. Web guidelines for FDM print design considerations.

[44] Michael Wüthrich, Maurus Gubser, Wilfried J. Elspass, and Christian Jaeger. A novel slicing strategy to print overhangs without support material. *Applied Sciences*, 11(18), 2021.

[45] Stefan Junk and Felix Bär. Design guidelines for additive manufacturing using masked stereolithography msla. *Procedia CIRP*, 119:1122–1127, January 2023.

[46] Carolyn Connor Seepersad, Tyler Govett, Kevin Kim, Michael Lundin, and Daniel Pinero. A designer's guide for dimensioning and tolerancing sls parts. 2012.

[47] Lara Rebaioli and Irene Fassi. A review on benchmark artifacts for evaluating the geometrical performance of additive manufacturing processes. *The International Journal of Advanced Manufacturing Technology*, 93(5):2571–2598, November 2017.

[48] Arghavan Farzadi, Mehran Solati-Hashjin, Mitra Asadi-Eydivand, and Noor Azuan Abu Osman. Effect of layer thickness and printing orientation on mechanical properties and dimensional accuracy of 3d printed porous samples for bone tissue engineering. *PLOS ONE*, 9(9):e108252, September 2014.

[49] Paramita Das, Ramya Chandran, Rutuja Samant, and Sam Anand. Optimum part build orientation in additive manufacturing for minimizing part errors and support structures. *Procedia Manufacturing*, 1:343–354, January 2015.

[50] A[di] Pandzic. Influence of layer height, build orientation and post-curing on tensile mechanical properties of sla 3d printed material. In B. Katalinic, editor, *Proceedings of the 32nd DAAAM International Symposium*, pages 0200–0208, Vienna, Austria, 2021. DAAAM International.

[51] Jingchao Jiang, Xun Xu, and Jonathan Stringer. Support structures for additive manufacturing: A review. *Journal of Manufacturing and Materials Processing*, 2(44):64, December 2018.

[52] Hai-ming Zhao, Yong He, Jian-zhong Fu, and Jing-jiang Qiu. Inclined layer printing for fused deposition modeling without assisted supporting structure. *Robotics and Computer-Integrated Manufacturing*, 51:1–13, June 2018.

[53] Ande Harshavardhan Reddy, Saritha Davuluri, and Dhatreyi Boyina. 3d printed lattice structures: A brief review. In *2020 IEEE 10th International Conference Nanomaterials: Applications Properties (NAP)*, pages 02SAMA10–1–02SAMA10–5, November 2020.

[54] Md Moniruzzaman, Christopher O'Neal, Ariful Bhuiyan, and Paul F. Egan. Design and mechanical testing of 3d printed hierarchical lattices using biocompatible stereolithography. *Designs*, 4(33):22, September 2020.

[55] Wenjin Tao and Ming C. Leu. Design of lattice structure for additive manufacturing. In *2016 International Symposium on Flexible Automation (ISFA)*, page 325–332, August 2016.

[56] Zuhal Ozdemir, Everth Hernandez-Nava, Andrew Tyas, James A. Warren, Stephen D. Fay, Russell Goodall, Iain Todd, and Harm Askes. Energy absorption in lattice structures in dynamics: Experiments. *International Journal of Impact Engineering*, 89:49–61, March 2016.

[57] Nan Jin, Fuchi Wang, Yangwei Wang, Zhang Bowen, Huanwu Cheng, and Hongmei Zhang. Failure and energy absorption characteristics of four lattice structures under dynamic loading. *Materials Design*, 169:107655, 02 2019.

[58] Paul F. Egan, Veronica C. Gonella, Max Engensperger, Stephen J. Ferguson, and Kristina Shea. Computationally designed lattices with tuned properties for tissue engineering using 3d printing. *PLOS ONE*, 12(8):e0182902, August 2017.

[59] Xiaojian Wang, Shanqing Xu, Shiwei Zhou, Wei Xu, Martin Leary, Peter Choong, M. Qian, Milan Brandt, and Yi Min Xie. Topological design and additive manufacturing of porous metals for bone scaffolds and orthopaedic implants: A review. *Biomaterials*, 83:127–141, March 2016.

[60] Shivani Sriya Ambati and Ravindra Ambatipudi. Effect of infill density and infill pattern on the mechanical properties of 3d printed pla parts. *Materials Today: Proceedings*, 64:804–807, January 2022.

[61] Thanh Tan Nguyen, Van Tron Tran, Van-Thuc Nguyen, and Van Thanh Tien Nguyen. Effect of infill ratios in sla 3d printing on mechanical properties of castable wax patterns for molded shells in investment casting. *PLOS ONE*, 20(2):e0311245, February 2025.

[62] B3D Group Sdn Bhd. Fff/fdm 3d print 101 — layer height, infill & support. Blog & News.

[63] Markéta Klimtová and Petr Veselý. Evaluation of anisotropy of additively manufactured structures. In *2021 44th International Spring Seminar on Electronics Technology (ISSE)*, page 1–6, May 2021.

[64] Olaf Diegel, Axel Nordin, and Damien Motte. *A Practical Guide to Design for Additive Manufacturing*. Springer Series in Advanced Manufacturing. Springer Singapore, Singapore, 2019.

[65] David Hernandez. Factors affecting dimensional precision of consumer 3d printing. *International Journal of Aviation, Aeronautics, and Aerospace*, 2(4), September 2015.

[66] Meltem Eryıldız. Effect of build orientation on mechanical behaviour and build time of fdm 3d-printed pla parts: An experimental investigation. *European Mechanical Science*, 5(33):116–120, September 2021.

[67] Sergio de la Rosa, Pedro F. Mayuet, José Ramón Méndez Salgueiro, and Lucía Rodríguez-Parada. Design of customized TPU lattice structures for additive manufacturing: Influence on the functional properties in elastic products. *Polymers*, 13(24):4341, 2021.

[68] Simon R. G. Bates, Ian R. Farrow, and Richard S. Trask. Compressive behaviour of 3d printed thermoplastic polyurethane honeycombs with graded densities. *Materials & Design*, 162:130–142, 2019.

[69] Fatah Habib, Pio Iovenitti, Syed Masood, Mostafa Nikzad, and Dong Ruan. Design and evaluation of 3d printed polymeric cellular materials for dynamic energy absorption. *The International Journal of Advanced Manufacturing Technology*, 102:2283–2296, 2019.

[70] Radosław Nowak, Dominik Rodak, Stefan Pytel, Przemysław Rumianek, Paweł Wawrzyniak, Daniel Krzysztof Debski, Agnieszka Dudziak, and Jacek Caban. Experiments and modeling of three-dimensionally printed sandwich composite based on ultem 9085. *Materials*, 17(21):5341, 2024.

[71] Hyojeong Lee, Rong-il Eom, and Yong Lee. Evaluation of the mechanical properties of porous thermoplastic polyurethane obtained by 3d printing for protective gear. *Advances in Materials Science and Engineering*, 2019:5838361, 2019.

[72] Miguel Davia-Aracil, Juan José Hinojo-Pérez, Antonio Jimeno-Morenilla, and Higinio Mora-Mora. 3d printing of functional anatomical insoles. *Computers in Industry*, 95:38–53, 2018.

[73] Sona Jandova and Radomir Mendricky. Benefits of 3d printed and customized anatomical footwear insoles for plantar pressure distribution. *3D Printing and Additive Manufacturing*, 9(6):547–556, 2022.

[74] Jing Zhang, Shikai Lu, Yifan Lin, Yao Wang, Xiaoxuan Yi, and Wen Fang. Pressure-reducing design of 3d-printed diabetic shoe midsole utilizing auxetic lattice structure. *Applied Sciences*, 14(12):5291, 2024.

[75] Lei Tang, Ling Wang, Wannan Bao, Siyao Zhu, Dong Li, Nana Zhao, and Chaozong Liu. Functional gradient structural design of customized diabetic insoles. *Journal of the Mechanical Behavior of Biomedical Materials*, 94:279–287, 2019.

[76] Silvia Badini, Stefano Regondi, Chiara Lammi, Chiara Bollati, Giacomo Donvito, and Roberto Pugliese. Computational mechanics of form-fitting 3d-printed lattice-based wrist–hand orthosis for motor neuron disease. *Biomedicines*, 11(7):1787, 2023.

[77] Carlo Boursier Niutta, Raffaele Ciardiello, and Andrea Tridello. Experimental and numerical investigation of a lattice structure for energy absorption: Application to the design of an automotive crash absorber. *Polymers*, 14(6):1116, 2022.

[78] P. Sharma and B. Bhattacharya. Parameter estimation of butyl rubber aided with dynamic mechanical analysis for numerical modelling of an air-inflated torus and experimental validation using 3d-laser doppler vibrometer. *ResearchGate*, 2019.

[79] T. Reppel and K. Weinberg. Mechanical characterization of fdm printed ninjaflex for engineering applications. *Technische Mechanik*, 39(1), 2019.

[80] V. S. Arutyunov et al. Mechanical properties and modeling of silicone rubber for prosthetic applications. *Plasma Physics Reports*, 47:1072–1079, 2021.

[81] ANSYS Inc. Ansys engineering data: Neoprene rubber material properties, 2024. ANSYS Material Library.

[82] L. R. G. Treloar. Stress-strain data for vulcanized rubber under various types of deformation. *Transactions of the Faraday Society*, 40:59–70, 1944.

[83] Ruben Bayu Kristiawan, Fitrian Imaduddin, Dody Ariawan, Ubaidillah, and Zainal Arifin. A review on the fused deposition modeling (fdm) 3d printing: Filament processing, materials, and printing parameters. *Open Engineering*, 11(1):639–649, January 2021.

[84] Mahtab Vafaeefar, Kevin M. Moerman, and Ted J. Vaughan. Experimental and computational analysis of energy absorption characteristics of three biomimetic lattice structures under compression. *Journal of the Mechanical Behavior of Biomedical Materials*, 151:106328, March 2024.

[85] Gerhard Pahl, Wolfgang Beitz, Jörg Feldhusen, and Karl-Heinrich Grote. *Engineering Design*. Springer, London, 2007.

[86] Angelina H. M. E. Reinders. Industrial design methods for product integrated pem fuel cells. 2006.

[87] Yang Song, Enze Shao, István Bíró, Julien Steven Baker, and Yaodong Gu. Finite element modelling for footwear design and evaluation: A systematic scoping review. *Heliyon*, 8(10):e10940, October 2022.

[88] Load Cell Central. Model rcd: Thru-hole load cell, n.d.

[89] Frank H. Netter. *Atlas of Human Anatomy*. Icon Learning Systems, Philadelphia, PA, 3 edition, 2002.

[90] John Y. Kwon, John T. Campbell, Mark S. Myerson, and Cliff L. Jeng. Effect of a steel toe cap on forefoot injury pattern in a cadaveric model. *Foot & Ankle International*, 32(4):443–447, 2011.

[91] C. Masson, L. Thollon, D. Cesari, and C. Brunet. Effects of static high compression on human foot-ankle: biomechanical response and injuries. *Surgical and Radiologic Anatomy*, 28(1):46–53, 2006.

[92] F. Xu, Y.S. Wong, H.T. Loh, J.Y.H. Fuh, and T. Miyazawa. Optimal orientation with variable slicing in stereolithography. *Rapid Prototyping Journal*, 3(3):76–88, 1997.

[93] L. Yang and M. A. Anam. An investigation of standard test part design for additive manufacturing. In *Proceedings of the 25th Annual International Solid Freeform Fabrication Symposium*, pages 901–922, Austin, TX, USA, 2014.

[94] Peter Zelinski. 7 helpful numbers quantify design rules for additive manufacturing. Blog post, *AdditiveManufacturing.*media, November 2016. Online; accessed via Proto Labs.

[95] Georgios Komineas, Panagiotis Foteinopoulos, Aristeidis Papacharalampopoulos, and Panagiotis Stavropoulos. Build time estimation models in thermal extrusion additive manufacturing processes. *Procedia Manufacturing*, 21:647–654, 2018.

[96] Shuvo Sikder, Ahmad Barari, and Hossam A. Kishawy. Effect of adaptive slicing on surface integrity in additive manufacturing. In *Proceedings of the ASME 2014 International Design Engineering Technical Conferences and Computers and Information in Engineering Conference (IDETC/CIE)*, volume 1A, Buffalo, NY, USA, 2014. ASME. 34th Computers and Information in Engineering Conference.

[97] Ramesh Chand, Vishal S. Sharma, Rajeev Trehan, Munish Kumar Gupta, and Murat Sarikaya. Investigating the dimensional accuracy and surface roughness for 3d printed parts using a multi-jet printer. *Journal of Materials Engineering and Performance*, 32(3):1145–1159, February 2023.

[98] Nor Aiman Sukindar, Ahmad Shah Hizam Md Yasir, Muhammad Danial Azhar, Muhammad Afif Md Azhar, Nor Farah Huda Abd Halim, Mohd Hafis Sulaiman, Ahmad Syamaizar Haji Ahmad Sabli, and Mohd Khairol Anuar Mohd Ariffin. Evaluation of the surface roughness and dimensional accuracy of low-cost 3d-printed parts made of pla–aluminum. *Heliyon*, 10(4):e25508, February 2024.

[99] D. Laumann, D. Spiehl, E. Dörsam, and A. Blaeser. Interaction of printing speed and temperature settings on the build plate adhesion of 3d-printed polylactide acid parts. *The Journal of Adhesion*, 99(7):1186–1204, May 2023.

[100] Hussein Alzyod and Peter Ficzere. Material-dependent effect of common printing parameters on residual stress and warpage deformation in 3d printing: A comprehensive finite element analysis study. *Polymers*, 15(1313):2893, January 2023.

[101] American National Standards Institute (ANSI) and International Safety Equipment Association (ISEA). American national standard for performance and classification for impact-resistant gloves (ansi/isea-138-2019). ANSI/ISEA-138-2019, 2019. Establishes test method, classification, and labeling requirements for dorsal (back-of-hand) impact protection.

[102] R. G. Craig, J. D. Eick, and F. A. Peyton. Strength properties of waxes at various temperatures and their practical application. *Journal of Dental Research*, 46(1):300–305, 1967.

[103] American National Standards Institute (ANSI) and International Safety Equipment Association (ISEA). American national standard for industrial head protection (ansi/isea-z89.1-2014, r2019), 2014. Reaffirmed 2019; Types I/II, Classes G/E/C impact and electrical protection.

[104] A Nugroho, R Ardiansyah, L Rusita, and I L Larasati. Effect of layer thickness on flexural properties of pla (polylactid acid) by 3d printing. *Journal of Physics: Conference Series*, 1130(1):012017, November 2018.

[105] Chang Liu, Zongliang Du, Weisheng Zhang, Yichao Zhu, and Xu Guo. Additive manufacturing-oriented design of graded lattice structures through explicit topology optimization. *Journal of Applied Mechanics*, 84(081008), June 2017.

[106] International Safety Equipment Association. Ansi/isea 138-2019: American national standard for performance and classification for impact-resistant gloves. Standard, 2019. ANSI/ISEA 138-2019, Arlington, VA.

[107] Arun Sharma and Bishakh Bhattacharya. Parameter estimation of butyl rubber aided with dynamic mechanical analysis for numerical modelling of an air-inflated torus and experimental validation using 3d-laser doppler vibrometer. *Journal of Low Frequency Noise Vibration and Active Control*, 38, 02 2019.